Linearized inversion frameworks toward high-resolution seismic imaging

By

Ali Aldawood

In Partial Fulfillment of the Requirements of

Doctor of Philosophy

Earth Sciences and Engineering Department
Physical Sciences and Engineering Division
King Abdullah University of Science and Technology, Thuwal,
Kingdom of Saudi Arabia

September, 2016

The thesis of Ali Aldawood is approved by the examination committee

Committee Chairperson: Ibrahim Hoteit

Committee Member: Tariq Alkhalifah

Committee Member: George Turkiyyah

Committee Member: Abdullatif Al-Shuhail

Committee Member: Mohammed Alfaraj

ABSTRACT

Linearized Inversion Frameworks toward High-resolution Seismic Imaging

Ali Aldawood

Seismic exploration utilizes controlled sources, which emit seismic waves that propagate through the earth subsurface and get reflected off subsurface interfaces and scatterers. The reflected and scattered waves are recorded by recording stations installed along the earth surface or down boreholes. Seismic imaging is a powerful tool to map these reflected and scattered energy back to their subsurface scattering or reflection points. Seismic imaging is conventionally based on the single-scattering assumption, where only energy that bounces once off a subsurface scatterer and recorded by a receiver is projected back to its subsurface position. The internally multiply scattered seismic energy is considered as unwanted noise and is usually suppressed or removed from the recorded data. Conventional seismic imaging techniques yield subsurface images that suffer from low spatial resolution, migration artifacts, and acquisition fingerprint due to the limited acquisition aperture, number of sources and receivers, and bandwidth of the source wavelet. Hydrocarbon traps are becoming more challenging and considerable reserves are trapped in stratigraphic and pinch-out traps, which require highly resolved seismic images to delineate them.

This thesis focuses on developing and implementing new advanced cost-effective seismic imaging techniques aiming at enhancing the resolution of the migrated images by

exploiting the sparseness of the subsurface reflectivity distribution and utilizing the multiples that are usually neglected when imaging seismic data. I first formulate the seismic imaging problem as a Basis pursuit denoise problem, which I solve using an L1-minimization algorithm to obtain the sparsest migrated image corresponding to the recorded data. Imaging multiples may illuminate subsurface zones, which are not easily illuminated by conventional seismic imaging using primary reflections only. I then develop an L2-norm (i.e. least-squares) inversion technique to image internally multiply scattered seismic waves to obtain highly resolved images delineating vertical faults that are otherwise not easily imaged by primaries.

Seismic interferometry is conventionally based on the cross-correlation and convolution of seismic traces to transform seismic data from one acquisition geometry to another. The conventional interferometric transformation yields virtual data that suffers from low temporal resolution, wavelet distortion, and correlation/convolution artifacts. I therefore incorporate a least-squares datuming technique to interferometrically transform vertical-seismic-profile surface-related multiples to surface-seismic-profile primaries. This yields redatumed data with high temporal resolution and less artifacts, which are subsequently imaged to obtain highly resolved subsurface images. Tests on synthetic examples demonstrate the efficiency of the proposed techniques, yielding highly resolved migrated sections compared with images obtained by imaging conventionally redatumed data.

I further advance the recently developed cost-effective Generalized Interferometric Multiple Imaging procedure, which aims to not only image first but also higher-order multiples as well. I formulate this procedure as a linearized inversion framework and solve it as a least-squares problem. Tests of the least-squares Generalized Interferometric Multiple imaging framework on synthetic datasets and demonstrat that it could provide highly resolved migrated images and delineate vertical fault planes compared with the standard procedure. The results support the assertion that this linearized inversion framework can illuminate subsurface zones that are mainly illuminated by internally scattered energy.

ACKNOWLEDGEMENTS

"No duty is more urgent than that of returning thanks." ∼ *James Allen*

To my supervisor, Prof. Ibrahim Hoteit, to you I express my sincere thanks.

I would never forget his warm welcome on my first day when I first joined his data assimilation group. His guidance and high expectations never seized to motivate and push me to work harder. His wide knowledge on many geophysical data inversion problems continued to enlighten me and really assisted me in finding solutions. I am grateful for his personal involvement and support with my business travel so I can present my work at prominent international conferences in Europe, United States, and the Middle East. I hope that our scientific collaboration continues for many years to come during my professional career.

My thanks are also extended to my sponsoring company, Saudi Aramco, for its solid commitments to develop its employee through higher education and training.

Heartfelt gratitude goes to my dissertation committee members, Prof. Tariq Alkhalifah and Prof. George Turkiyyah. Dr. Alkhalifah's deep knowledge and understanding of wave-propagation physics and seismic imaging and inversion helped me pursue my desired research direction whereas Dr. Turkiyyah's computational and optimization knowledge helped me execute my proposed solutions and be more efficient in the optimal direction of research. I would also like to take the opportunity to thank my external collaborators, Prof. Abdullatif Alshuhail and Dr. Mohammed Alfaraj. Their personal and technical advises helped me strengthen my research base and overcome many obstacles.

I am thankful to my teachers, friends, cousins, and KAUST colleagues; namely Mo-

hammad Zuberi whose earlier work has become the base of my thesis dissertation topic.

“A happy family is but an earlier heaven.” John Bowring.

To my parents, all my achievements and successes would not have been possible without my parents’ love, prayers and endless support. I can never thank them enough. I dedicate this dissertation and my success to them.

TABLE OF CONTENTS

LIST OF ABBREVIATIONS

BPDN	Basis Pursuit denoise
CDP	common-depth-point
CS	Compressed Sensing
FWI	Full Waveform Inversion
GIMI	Generalized Interferometric Multiple Imaging
HPC	high performance computing
L-BFGS	limited memeory BFGS
LSD	Least-squares Datuming
LSM	Least-squares Migration
MVA	migration velocity analysis
RTDM	reverse time demigration
RTM	reverse time migration
SNR	signal-to-noise ratio
SPGL1	spectral projected gradient algorithm
SSP	Surface-Seismic-Profiling
VSP	Vertical-Seismic-Profiling

LIST OF FIGURES

Chapter 1

Introduction

1.1 Background

Finding hydrocarbon traps is increasingly becoming a more challenging problem. Explorationists, nowadays, are targeting small scale structural and pinch out traps. Locating small scale faults and stratigraphic traps requires highly resolved migrated seismic images for interpretation purposes. These migrated images are obtained by placing the recorded reflected seismic energy along the recording surface in its true subsurface position. Conventional imaging algorithms utilize primary reflections that are reflected only once from a subsurface scatterer before it is recorded by a receiver along the recording surface. These single-bounce recorded events are imaged to obtain an estimate of the subsurface reflectivity distributions (i.e., subsurface structures). However, the surface records often contain multiple-scattered energy that is considered as undesired noise and is usually suppressed by one or more seismic processing algorithms prior to imaging. The reason is that conventional migration algorithms are only designed to take single-scattering (i.e., primary) reflections into account (Wapenaar et al., 2015). Therefore, applying conventional single-scattering migration in the presence of seismic multiples would deteriorate the quality of the final image as the multiple events are placed in wrong subsurface positions by the imaging algorithm. Conventional imaging techniques yield migrated sections that suffer from migration artifacts, cross-talk noise, and low spatial resolutions. They are also based on the single-scattering assumption; therefore, they may not illuminate subsurface features that are illuminated by internal multiples. Therefore, the motivation of this work is to develop and test new cost-efficient migration and inversion technologies exploiting the sparsity nature of the subsurface reflectivity distribution or utilizing the surface-related and/or internal multiple energy, which could potentially provide highly resolved migrated sections.

The goal of seismic migration is to map, using a migration velocity model, observed seismic data at recording stations along the earth surface or down boreholes into representative subsurface structures (Claerbout, 1971). Mathematically, the seismic imaging problem can be posed as an inversion problem to find the best subsurface reflectivity model that explains the recorded data. The forward problem yields seismic data given a velocity and a reflectivity model. Direct solvers are prohibitively expensive to use in solving the seismic inversion problem (Dai, 2012). Therefore, the seismic inversion problem is conventionally solved iteratively by applying a pair of forward and adjoint operators that are based on the wave-equation. While the forward operator is used to compute the seismic data to be compared with the observed data, the adjoint operator is used to back-project the residual in order to update the seismic image through iterations. LeBras and Clayton (1988) and Nemeth et al. (1999) proposed a linearized inversion or Least-squares Migration (LSM), which is an iterative scheme to invert seismic data to representative subsurface reflectivity distribution. LSM is a special form of Full Waveform Inversion (FWI) which only inverts for a high wavenumber reflectivity model (i.e., the migrated image) whereas FWI tries to update both the reflectivity model and the background velocity model that describes the wave propagation in the subsurface (Luo et al., 2013). Thus, least-squares migration can be considered as a cost-effective linearized waveform inversion as it does not require the extrapolation of the new wavefields, but only the update of the migrated images at each iteration. LSM requires an accurate migration velocity estimate to accurately predict the kinematics of of the wave propagation in the subsurface (Luo et al., 2013; Dutta et al., 2014).

LSM can improve the seismic image quality by suppressing the migration artifacts, enhance the spatial resolution of the migrated section, and compensate for the acquisition footprint and amplitude loss (LeBras and Clayton, 1988; Nemeth et al., 1999; Khl and Sacchi, 2003; Dai, 2012; Luo et al., 2013). The fact that the LSM method minimizes the sum of the squares of the residuals to find the least-squares solution, makes it intrinsically yield smooth solutions (Abubakar et al., 2005; Tang, 2006; Liu et al., 2011a; Borsic and Adler, 2012). Although adding a regularizing term to the objective function may further suppress migration artifacts and sharpens the least-squares image, most regularization terms assume that the inverted model parameters are smooth and continuous, further smoothing the final inverted migrated section (Aster et al., 2005). Therefore, imposing a regularization term that does not further smooth the reflectivity distribution but rather promotes its sparseness, such as the L1-norm constraint, can help enhance the spatial resolution of the migrated subsurface structures. In this dissertation, I develop and implement different methods to extend the idea of least-squares migration in attempts to obtain highly resolved images. I first recast the classical least-squares migration problem as a compressive sensing (i.e. sparse reconstruction) problem known as the Basis Pursuit denoise (BPDN) problem (Chen et al., 1998). Given that the seismic reflection events from the subsurface are sparse, the solution of this problem yields a highly resolved sparse image that could explain the recorded seismic data.

However, imaging primaries intrinsically illuminates horizontal reflectors but hardly illuminates vertical reflectors such as vertical and nearly vertical faults, or salt flanks (Verschuur and Berkhout, 2015; Berkhout and Verschuur, 2016). Thus, utilizing internal multiples could potentially illuminate vertically lying subsurface reflectors. FWI is known to provide highly resolved images but the computation of the FWI gradient is based on the single-scattering assumption. The gradient of FWI is computed using a similar procedure as the standard pre-stack migration image of primary reflections (Pratt, 1999; Nemeth et al., 1999). Thus, although the modeling step in FWI can generate both surface-related and internal multiples in the modeling step, its conventional adjoint is based on the single-scattering assumption (i.e., the Born approximation) and this limits its ability to delineate reflectors that are mainly illuminated by internally multiplied waves. In conventional migration, primaries are enhanced by several seismic processing steps as the migration is based on the single-scattering assumption (i.e. imaging primaries only) while multiples are normally suppressed or removed since they are not accounted for by conventional imaging algorithms. Exploiting multiples will be proven to be a key tool to obtain highly resolved seismic images and to widen the subsurface illumination (Hanafy et al., 2015). Both internal and surface-related multiples can provide wider subsurface illumination (Sheng, 2001; Guitton, 2002; Muijs et al., 2005; Zuberi and Alkhalifah, 2014a; Yang et al., 2015; Guo et al., 2015). Recently, Wong et al. (2014); Tu and Herrmann (2015) applied least-square migration algorithms to image the subsurface with surface-related multiples and obtained subsurface images with enhanced illumination. Inverting for internal multiples, however, can be quite challenging as the internally scattered waves are weaker and can be obscured by the stronger primaries and surface-related multiples (Verschuur and Berkhout, 2015). Verschuur and Berkhout (2015) showed that whereas surface-related multiples can be separated and imaged using linearized inversion (closed-loop) frameworks, isolating internal multiples is quite challenging as they are an integral part of the total wavefield. In this dissertation, I propose a linearized inversion or least-squares migration framework to image internal multiples in an attempt to locate vertical fault planes that are not easily illuminated by primaries. However, the modeling of internal multiple data in a linearized framework setting can be quite expensive as it requires a nested summation over the model space in the proposed framework. It also requires an accurate estimate of the subsurface reflectivity distribution obtained by inverting primaries. Therefore, I resort to the recently developed Generalized Interferometric Multiple Imaging (GIMI) procedure which has a computational cost similar to that of imaging primaries (Zuberi and Alkhalifah, 2014b). The GIMI procedure is an imaging technique, which means that an adjoint operation is applied to migrate first-order, or even higher order internal multiples, to obtain an approximate reflectivity distribution of the subsurface. The power of this method lies in its ability to image the internal multiples selectively and automatically without the requirement for multiple separation. However, its major drawback is that it is an imaging procedure (i.e. adjoint operation) and is not an inversion-based framework, which requires the derivation of a forward modeling operator to predict the internal multiples. In this dissertation, I propose to improve this procedure by formulating it as a linearized inversion problem, which requires the derivation of a modeling operator (i.e., adjoint of the GIMI adjoint) to predict the first-order, or higher order multiple data along the recording surface. To formulate this adjoint, I first investigate the idea of least-squares interferometric datuming in Chapter 4 since the modeling and datuming operators of interferometric datuming will be the building blocks to the least-squares GIMI procedure in Chapter 5.

Seismic interferometry, also known as the virtual source method, is widely used to transform seismic data from one acquisition geometry to another by creating virtual sources or receivers where there are no recording stations or shot points in the actual acquisition geometry (Curtis et al., 2006; Broggini et al., 2011; Boullenger* and Draganov, 2015). The engines of this method are the reciprocity equations of the convolution and correlation type where the recorded traces are used as natural wavefield extrapolators (Wapenaar and Fokkema, 2006; Schuster, 2009). The limitation of the conventional cross-correlation or convolution based interferometric datuming is that they yeild redatumed data that suffers from low temporal resolution and is contaminated by the redatuming artifacts. In Chapter 4 of this dissertation, I apply a Least-squares Datuming (LSD) framework to convert surface-related Vertical-Seismic-Profiling (VSP) multiples into virtual Surface-Seismic-Profiling (SSP) primaries. The correlation and convolution based datuming operators are used as a pair of an adjoint and forward modeling operators in this linearized inversion framework. The least-squares datumed data are subsequently imaged to extend the subsurface imaging aperture and enhance the resolution of the final migrated section. Based on the LSD framework, I then extend the GIMI methodology and formulate it as a linearized inversion framework in order to obtain highly resolved images and localize a vertical fault plane when imaging first-order internal multiples. The GIMI procedure consists of a series of extrapolation-based and correlation-based datuming steps followed by an imaging step. Thus, the modeling and adjoint operators utilized for least-squares datuming are shown to be the building blocks to find a corresponding adjoint (i.e., modeling operator) of the GIMI procedure as each of its datuming steps can be regarded as a least-squares datuming subproblem.

1.2 Thesis Objectives and Contributions

The main objective of this dissertation is to exploit the sparsity nature of the subsurface reflectivity distribution when inverting the primary reflections to obtain highly resolved migrated images, and to utilize both surface-related and internal multiples in linearized inversion frameworks to widen the subsurface illumination for improved imaging of subsurface reflectors, which are not easily illuminated by primary reflected energy. I intend to tackle these problems in this dissertation in the following chapters:

- In Chapter 2, I apply a compressed sensing algorithm to solve the seismic imaging of primary reflections problem as an L1-norm minimization problem instead of the conventional L2-norm minimization (i.e., least-squares) problem. I formulate the objective function such that I impose a constraint that promotes the sparseness of the model parameters (i.e., reflectivity distributions) by minimizing the L1 norm of the reflectivity model at each iteration of the linearized inversion framework. The goal is to test on synthetic data the ability of the compressed sensing migration in obtaining highly resolved migration images when imaging primaries.

- Although compressive sensing migration can provide highly resolved images of the subsurface as demonstrated in Chapter 2, it fails to accurately delineate vertical and nearly vertical reflectors as they are not well illuminated by primaries. In Chapter 3, I develop a linearized inversion algorithm to invert internal multiples and obtain subsurface images with wider subsurface illumination. I thus apply a linearized inversion, or least-squares migration, framework to image internally-multiplied seismic energy. The objective is to localize vertical fault planes that are not easily illuminated by primaries, but could be well-illuminated by doubly-scattered seismic energy. Modeling first-order internal multiples is a non-linear operation and requires a nested summation in which the reflectivity functions are multiplied at two different points inside the model. I first linearize this modeling process by setting one of the multiplied terms to be the fixed image obtained by the least-squares migration of primaries. I then derive the corresponding adjoint linear operator that maps first-order multiples into subsurface reflectors, which are mainly illuminated by doubly-scattered waves. Nevertheless, the linearized modeling step is still computationally expensive as it requires a nested summation over the model space. Thus, I propose to extend the more computationally-efficient GIMI procedure to image first-order or higher order internal multiples, which does not require the double summation over the model space. The engines of the GIMI procedure are cross-correlation, or extrapolation, based datuming steps. I thus utilize in Chapter 3 the least-squares datuming in a VSP geometry when imaging surface-related multiples as it will be the building framework to formulate a linearized inversion version of the GIMI procedure.

- In Chapter 4, I propose and test a least-squares datuming framework to convert VSP surface-related multiples into SSP primaries by utilizing seismic interferometry, also known as the virtual source method. I use the cross-correlation based datuming to remove the propagation path from a source point along the Earth surface and recorded by VSP station. In other words, I use the interferometric transformation to transform a VSP surface-related multiple into a virtual surface seismic primary. The corresponding adjoint is of convolution type in which I convolve the virtual primary with the direct wave from the Earth surface to the VSP recording station in order to predict the VSP surface-related multiples. The correlation based datuming and the corresponding convolution based datuming steps are formulated as a linearized inversion problem to obtain the optimal virtual SSP data that explains the synthetic recorded VSP data.

- In Chapter 5, I apply a least-squares GIMI frameworks to synthetic data examples to image subsurface scatterers and a vertical fault plane. The first two steps of the GIMI procedure is an extrapolation-based datuming and a correlation-based datuming. I utilize the derived operators in Chapter 4 and turn these datuming steps into least-squares datuming subproblems, which can be used to enhance the quality of the redatumed data prior to imaging first-order internal multiples by the third GIMI step. The goal is to enhance the spatial resolution of the migrated GIMI images and suppress the artifacts that arise from the extrapolation and cross-correlation datuming steps in the GIMI procedure.

- In Chapter 6, I summarize the main results of this dissertation and propose a road map for future work that would improve the proposed cost-effective linearized inversion frameworks in this dissertation. I also list the major scientific contributions of this dissertation including conference papers and peer-reviewed journal papers.

Chapter 2

The Possibilities of Compressed-sensing based Kirchhoff pre-stack Migration

An approximate subsurface reflectivity distribution of the Earth is usually obtained through the migration process. However, conventional migration algorithms, including those based on the least-square approach, yield structure descriptions that are slightly smeared and of low resolution caused by the common migration artifacts due to limited aperture, coarse sampling, band limited source, and low subsurface illumination. To alleviate this problem, I utilize the fact that minimizing the L1-norm of a signal promotes its sparsity. Thus, I formulate the Kirchhoff migration problem as a compressed-sensing Basis Pursuit denoise problem to solve for highly focused migrated images compared with those obtained by standard and least-square migration algorithms. The results of various subsurface reflectivity models show that solutions, which are computed using the compressed-sensing based migration, provide more accurate subsurface reflectivity location and amplitude. I applied the compressed-sensing algorithm to image synthetic data from a fault model using dense and sparse acquisition geometries. The results suggest that the proposed approach may still provide highly resolved images with a relatively small number of measurements. I, also, demonstrate the robustness of the Basis Pursuit denoise algorithm in the presence of Gaussian random observational noise and in the case of imaging the recorded data with inaccurate migration velocities.

2.1 Introduction

Seismic imaging using Kirchhoff-type integrals, which is based on high frequency asymptotic solutions to the wave-equation, is a powerful tool to map the data recorded on the surface of the Earth into representative subsurface structures. However, a major drawback of standard Kirchhoff migration is that it suffers from migration artifacts, which results in a blurred depiction of the true subsurface reflectivity distributions. This effect is primarily caused by the limited acquisition aperture, coarse source-receiver sampling, band-limited source wavelet, and low subsurface illumination (Nemeth et al., 1999; Tang, 2009).

Least square migration has the potential to retrieve the subsurface reflectivity series more accurately than standard migration. LSM is used to reduce the migration artifacts and enhance the spatial resolution of the migrated image (LeBras and Clayton, 1988; Nemeth et al., 1999). It provides an approximate solution for the subsurface reflectivity as demonstrated by the linearized waveform inversion (Landa et al., 1989; Crase et al., 1990; Snieder et al.; Roth and Tarantola)

Adding a regularization term in the objective function may suppress the migration artifacts and sharpen the subsurface reflectivity distribution (Fomel and Guitton, 2006). Most regularization techniques assume that the inverted model parameters are smooth and continuous (Aster et al., 2005). However, since the reflectivity distribution (i.e. the model parameter) is sparse and discontinuous, I could formulate the Kirchhoff migration problem as a compressed-sensing problem, which could be solved using L1-minimization algorithms.

Compressed Sensing (CS), or sparse recovery, is an emerging field that is widely used to solve linear systems when the desired signal is sparse (Donoho, 2006; Eldar and Kutyniok, 2012). It relies on the fact that many signals or images can be well-approximated by a linear combination of suitable basis or dictionaries (e.g. Fourier, or wavelets) with only a small number of non-zero coefficients (Donoho, 2006). JPEG, MP3 are typical examples of these lossy compressions where only large basis coefficients are stored and the rest are set to zero (Pennebaker and Mitchell, 1992; Taubman and Marcellin, 2002).

The power of compressed sensing lies in its ability to reconstruct a compressed version of the original signal while requiring only a small number of measurements. Clearly, this could lead to a very important saving in both data collection and computational time. For example, the implementation of the compressed-sensing technology resulted in a speedup factor of seven times in obtaining pediatric MRI while preserving the diagnostic quality (Lustig et al., 2005, 2006; Trzasko and Manduca, 2009).

In this chapter, I first present the theory of least-square migration. I next formulate the migration problem as a Basis Pursuit denoise problem (i.e. L1-minimization problem) and solve it to try to retrieve the sparsest reflectivity distribution that explains the recorded data. The objective of this work is to spatially focus the migrated image, and reduce the smearing effect caused by the least-square minimization. I also study whether I can accurately recover a highly resolved subsurface image using a smaller number of measurements while deploying fewer sources and receivers. I finally study the robustness of the compressed-sensing approach focusing on the retrieval of spatially focused migrated images with reduced migration artifacts in the presence of white Gaussian random noise and in the case of migrating the data using erroneous migration velocity.

2.2 Least-square migration

The Kirchhoff forward modeling operator $\mathbf{L}$ maps the subsurface reflectivity distribution to scattered seismic data. Generating synthetic seismic data by Kirchhoff modeling can be represented by a matrix-vector multiplication as:

$$\mathbf{d} = \mathbf{L}\mathbf{m}, \tag{2.1}$$

where $\mathbf{d}$ is the modeled scattered seismic data and $\mathbf{m}$ is the true subsurface reflectivity distribution. A standard migrated image is obtained by applying the adjoint of the forward modeling operator (Claerbout, 1992):

$$\mathbf{m_{mig}} = \mathbf{L^T}\mathbf{d}, \tag{2.2}$$

where $\mathbf{m_{mig}}$ is the migrated image. Substituting the expression of $\mathbf{d}$ in equation (3.1) into equation (3.3) yields:

$$\mathbf{m_{mig}} = \mathbf{L^T}\mathbf{L}\mathbf{m}, \tag{2.3}$$

where $\mathbf{L^T}\mathbf{L}$ is known as the model resolution matrix and reflects the amount of smearing in the seismic image resulting from many factors, including limited recording aperture. The physical interpretation of the model resolution matrix is that the standard migrated image is a linear combination of the true reflectivity model. The Kirchhoff forward operator and its corresponding adjoint operator in their explicit discrete form are given as:

$$\mathbf{d}(s,g,t) = [\mathbf{L}\mathbf{m}]_{s,g,t} = \beta \sum_{\mathbf{x}} w(t - \tau_{s\mathbf{x}} - \tau_{\mathbf{x}g})\mathbf{m}(\mathbf{x}), \tag{2.4}$$

$$\mathbf{m}(\mathbf{x}) = [\mathbf{L^T d}]_{\mathbf{x}} = \sum_s \sum_g \sum_t w(t - \tau_{s\mathbf{x}} - \tau_{\mathbf{x}g})\mathbf{d}(s, g, t), \tag{2.5}$$

where s, g, $\mathbf{x}$, and t are the source position, receiver position, trial image point, and time sample, respectively. $\tau_{s\mathbf{x}}$ is the travel time from the source position s to the trial image point $\mathbf{x}$. Similarly, $\tau_{\mathbf{x}g}$ is the travel time from the trial image point $\mathbf{x}$ to the receiver position g. β is an amplitude factor that describes the geometrical spreading of the wave. As one may note, the summation is over the model space $\mathbf{x}$ for modeling seismic data whereas it is over the data space s, g, and t for migrating recorded data. The migration operators are adjoint operators of the forward modeling ones as they *undo* the time and phase shifts of the modeling operators but do not divide the color (i.e. account for the amplitude) (Claerbout and Fomel, 2008).

Least-square migration yields an approximate reflectivity image that minimizes the sum of the squares of the residual vector. Mathematically, the unconstrained objective function is defined as:

$$J = \|\mathbf{Lm} - \mathbf{d}\|_2 = \mathbf{m^T L^T L m} - \mathbf{2 m^T L^T d} + \mathbf{d^T d}. \tag{2.6}$$

The minimizer of this objective function is found by taking the gradient with respect to $\mathbf{m}$ and setting it to zero:

$$\nabla_{\mathbf{m}} J = \mathbf{L^T L m} - \mathbf{L^T d} = 0. \tag{2.7}$$

Hence, a more accurate solution to the migration problem is obtained by solving equation (3.7) which is the so-called normal equation:

$$\mathbf{L^T L m_{mig}} = \mathbf{L^T d}. \tag{2.8}$$

Gradient-based algorithms are generally used to solve this equation iteratively where data residuals are imaged to obtain model updates. By re-arranging the terms in equation (3.7), the gradient at every iteration is given by:

$$\nabla_{\mathbf{m}} J = \mathbf{L^T}(\mathbf{Lm} - \mathbf{d}) = \mathbf{L^T r}, \tag{2.9}$$

where $\mathbf{r}$ is the data residual vector. The pseudo code for the gradient-descent algorithm is as follows:

```
$while(\|\mathbf{g^k}\| \ is \ large)$
$\mathbf{g^{k+1}} = \mathbf{L^T}(\mathbf{Lm^k} - \mathbf{d})$
$\mathbf{m^{k+1}} = \mathbf{m^k} - \alpha\mathbf{g^{k+1}}$
$k = k + 1$                                        (2.10)
$end.$
```

The gradient $\mathbf{g^k}$ is obtained by back-projecting the data residual vector using the adjoint of the Kirchhoff forward modeling operator. At each iteration k, the reflectivity vector $\mathbf{m}$ is updated by moving along the negative gradient direction (i.e. the steepest descent direction) and the scalar quantity α is the step length that determines how much one can move along that direction. The step length is calculated using the following formula (Claerbout and Fomel, 2008):

$$\alpha = \frac{\mathbf{r^T \Delta r}}{\mathbf{\Delta r^T \Delta r}}, \tag{2.11}$$

where $\mathbf{r} = \mathbf{Lm} - \mathbf{d}$ and $\mathbf{\Delta r} = \mathbf{L \Delta m}$.

Although least-square migration suppresses the migration artifacts and helps focus the migrated image, this L2-norm minimization tends to produce a smeared version of the true reflectivity distribution (Avron et al., 2010; Yu et al., 2011). Thus, a major limitation of least-square migration is that it tends to produce images with limited bandwidth partially due to the band-limited nature of the source wavelet (Ribodetti et al., 2011).

2.3 Compressed sensing

Since the subsurface reflectivity distribution is known to be sparse and discontinuous, compressed sensing can be utilized to produce highly resolved migrated images from the given data where the migration artifacts are significantly compressed. The sparsest reflectivity distribution is found by solving the following L0-optimization problem (Donoho, 2006):

$$min \; ||\mathbf{m}||_0 \; subject \; to \; \mathbf{Lm} = \mathbf{d}, \tag{2.12}$$

where $||\mathbf{m}||_0$ counts the number of non-zero elements in the vector $\mathbf{m}$. This optimization problem has a non-convex objective function, and is NP-hard and intractable as it requires an exhaustive combinatorial search to find the solution. Nevertheless, the L0-norm can be relaxed to the L1-norm leading to a convex optimization problem that is computationally tractable (Chen et al., 2001):

$$min \; ||\mathbf{m}||_1 \; subject \; to \; \mathbf{Lm} = \mathbf{d}. \tag{2.13}$$

This L1-minimization problem is known as the Basis Pursuit approach, which is used to reconstruct sparse signals. Chen et al. (2001) showed that this L1-optimization problem can be cast as a linear program. However, in the presence of noise, this constraint cannot be exactly satisfied. In other words, there is no feasible $\mathbf{m}$ that perfectly maps to the recorded scattered data $\mathbf{d}$. Hence, I reformulate the Basis Pursuit problem as a BPDN problem which is defined as (van den Berg and Friedlander, 2008):

$$min \; \|\mathbf{m}\|_1 \; subject \; to \; \|\mathbf{Lm} - \mathbf{d}\|_2 < \sigma, \tag{2.14}$$

where the tolerance σ is a non-negative small scalar. van den Berg and Friedlander (2007) presented an algorithm that solves this problem for any tolerance value. They showed that there is a trade-off curve between the two objectives: minimizing the least-square data fitting and minimizing the L1-norm of the solution that promotes sparsity. Therefore, giving more weight to the data fitting is only feasible at the expense of getting a less sparse solution and vice versa. This curve is known as the Pareto optimal curve and van den Berg and Friedlander (2008) showed that this curve is convex and continuously differentiable over all points of interest. They claim that their root-finding algorithm can find arbitrary point on the Pareto optimal curve.

van den Berg and Friedlander (2007) basically cast the BPDN problem as a problem of finding the root of a single-variable nonlinear equation $\phi(\tau) = \sigma$ parameterizing the Pareto curve. At each iteration, an estimate of τ is used to define a convex optimization problem (i.e. LASSO problem) whose solution yields function and derivative information that are next used by a Newton-based root-finding algorithm to probe the Pareto curve. The goal is to find the optimal trade-off between the two competing objectives. van den Berg and Friedlander (2007) proposed a spectral projected gradient algorithm (SPGL1) that iteratively solves a sequence of LASSO problems of the form:

$$min \; \|\mathbf{Lm} - \mathbf{d}\|_2 \; subject \; to \; \|\mathbf{m}\|_1 < \tau. \tag{2.15}$$

SPGL1 is a free Matlab package which implements van den Berg and Friedlander (2007) algorithm and I utilized it to solve the Kirchhoff imaging problem. At each iteration, the algorithm uses the forward modeling operator in equation (2.4) to model the scattered data. Then, the adjoint operator in equation (2.5) is used to back-project the residual vector to compute the gradient direction as in equation (3.9), and consequently a gradient-based model update. The new iterate is then projected orthogonally onto the L1-norm unit ball of size τ in order to promote the sparsity of the solution.

2.4 Single scatterer example

In this example, the grid spacings of this 75 by 75 grid are $\Delta x = \Delta z = 7$ meters, and the time sampling is 2 ms. A point scatterer of unit amplitude is placed at the center of the model shown in Figure 3.2(a) and the background velocity model is constant and equals to 1000 m/s. I generated 75 noise-free shots located at the surface by Kirchhoff forward modeling operator using a Ricker wavelet with a peak frequency of 20 Hz. The acquisition geometry and parameters for this example and the other examples are quite similar. The first shot is at the top-left corner and the last shot is at the top-right corner. The remaining equally spaced shots are placed at the grid points along the Earth surface. Similarly, there are 75 equally spaced receivers placed at the grid points along the Earth surface.

The standard migrated image is obtained by applying the adjoint of the forward modeling operator to the shot gathers and it is shown in Figure 3.2(b). Clearly, the standard migrated image is a blurred version of the true subsurface reflectivity model. Even though the standard migrated image roughly indicates the position of the scatterer, the amplitude of the scatterer is very far from the true one. The migration artifacts (i.e. smiles) deteriorate the quality of the image.

On the other hand, the least-square migration result in Figure 3.4(a) shows a considerable enhancement of the image quality and mitigation of the migration artifacts after 30 gradient descent iterations. Also, this linearized inversion yielded a scatterer amplitude of about 0.25 compared with the true amplitude of 1. The least-square solution is still a smooth version of the true subsurface reflectivity model and that explains the smearing effect in Figure 3.4(a).

Therefore, I try to retrieve a sparse representation of the reflectivity image using compressed sensing. The compressed-sensing solution, obtained by solving the Basis Pursuit denoise problem, promotes the sparsity of the subsurface reflectivity distribution as shown in Figure 2.1(d). With a value of $\sigma = 1 \times 10^{-4}$, the compressed-sensing solution shows dramatic removal of the migration artifacts and the scatterer is localized at its true position after 8 iterations. Also, the amplitude of the scatterer is closer to the true one and it is found to be around 0.87.

2.5 Horizontal layers example

In this example, the grid spacing $\Delta x = \Delta z = 7$ meters, and the time sampling is 2 ms. Also, the velocity model of this example is shown in Figure 2.2(a). The problem is to recover a subsurface Earth model that consists of three horizontal interfaces with three different reflectivity values (0.5, 0.25, and 0.1) as shown in Figure 3.3(a). I generated 75 shots using the Kirchhoff forward modeling operator along the surface using a Ricker wavelet of a dominant frequency of 60 Hz.

The standard migration image resulted in a blurred version of the true subsurface image as shown in Figure 3.3(b). This is caused by smearing the recorded data over the corresponding migration operator in the image domain (i.e. smearing the recorded event over all possible reflection points). Since I only deployed 75 shots and 75 receivers along the surface, this image is heavily smeared and dominated by the migration smiles leading to this fuzzy depiction of the true reflectivity model. Also, the quality of the migrated image deteriorates considerably near the edges of the model due to the limited acquisition coverage; hence, these regions are dominated by migration artifacts.

To alleviate these problems, least-square migration is applied to migrate the data and the result in Figure 3.4(b) shows the mitigation of the migration artifacts, and the enhancement of both image quality and the resolution of the reflectors after 30 gradient descent iterations. Furthermore, least-square solution partially resolves the reflectors close to the edges of the model and partially compensates for the low illumination near these areas. Nevertheless, least-square migration still provides a smooth solution whereas the true reflectivity distribution is sparse and discontinuous. Note that there exist some spurious artifacts (i.e. events) in the vicinity of each reflector. Also, the amplitude of each reflector is weaker than the true one because the energy is still spread over several depth samples close to the reflector.

The compressed-sensing solution is obtained by iteratively solving the Basis Pursuit denoise problem and is shown in Figure 2.2(e). After 30 iterations and using a value of $\sigma = 1 \times 10^{-4}$, this sparse solution shows that the migration artifacts, especially at the edges, are significantly reduced. Also, the amplitude of each reflector is better recovered than the smooth least-square solution, especially away from the low coverage areas close to the edges of the model.

2.6 Fault model example

In this example, the grid spacing $\Delta x = \Delta z = 10$ meters, and the time sampling is 2 ms. I computed the standard, unconstrained least-square, and compressed-sensing solutions for a fault model of the Earth. Both the velocity model and the true reflectivity model are shown in Figure 2.3(a) and Figure 2.3(b), respectively. I generated 75 noise-free shots using the Kirchhoff forward modeling operator along the surface using a Ricker wavelet of a dominant frequency of 20 Hz.

The standard migration imaging computed a heavily blurred depiction of the true subsurface image as shown in Figure 2.3(c). In fact, it is quite hard to interpret and estimate an accurate position of the fault plane from this image. Moreover, the poor illumination and the limited acquisition aperture worsen the migrated image quality near the edges of the model.

Applying unconstrained least-square migration to the synthetic data enhances the image quality. One could now delineate the position of the fault plane after 30 gradient descent iterations as clearly seen in Figure 2.3(d). However, I managed to preserve the sparsity nature of the migrated image by solving the Basis Pursuit denoise problem and the solution after 30 iterations is shown in Figure 2.4(a). By choosing $\sigma = 4 \times 10^2$, this sparse solution resolves the events spatially more accurately with more precise amplitude information than the smooth least-square solution.

An interesting challenge is to find out if one can reconstruct an accurate representation of the subsurface reflectivity model using a fewer number of measurements. For this matter, I significantly reduced the number of sources and receivers by a factor of 5 compared with the previous case (i.e. utilizing only 4% of the available data). In this case, there are only 15 shots and 15 receivers equally spaced along the surface. The first shot is placed at the top left corner grid point of the model and the last one is located at top right corner. The spacing interval between sources and also receivers is now 50 meters instead of 10 meters in the dense geometry.

While the common-depth-point (CDP) sampling is 5 meters in the dense geometry, it is 25 meters in this sparse acquisition geometry. In the fault model, the velocity ranges from 2000 m/s to 3500 m/s. With a dominant frequency of 20 Hz, the dominant wavelength ranges from 100 m to 175 m. Using the dense geometry, I sampled the image point at 20 to 30 points per wavelength, which is quite dense. On the other hand, with the sparse acquisition geometry, the imaging point is sampled at only 4 to 7 points per wavelength.

The compressed-sensing solution using the new geometry is shown in Figure 2.4(b) and it is remarkably better than the standard migrated image and the least-square image using the dense geometry shown in Figure 2.3(c) and Figure 2.3(d), respectively. The compressed-sensing solution using the sparse geometry is quite comparable with the compressed-sensing one using the dense acquisition geometry shown in Figure 2.4(a) even though the image is slightly blurred and the amplitude information of the reflectors becomes less accurate. Hence, with only 4% of the available data and resources, compressed sensing managed to retrieve a highly focused migrated image. The computational time is reduced significantly compared to computing solutions with the dense acquisition geometry.

I also tested the compressed-sensing based imaging using a more sparse acquisition geometry. In this test, there are only 5 shots and 5 receivers equally spaced along the earth surface. Similarly, the first shot is placed at the top left corner grid point of the model and the last one is located at top right corner. Also, the spacing interval between shots and between receivers is now 150 meters; hence, the CDP sampling is 75 meters. Therefore, the imaging point is sampled only at around 1 to 2 points per wavelength. The capability of compressed-sensing migration deteriorates heavily in this very sparse acquisition geometry as shown in Figure 2.4(c). Thus, the compressed-sensing imaging requires sufficient CDP sampling of the imaging point to be able to focus the scatterers in their accurate positions.

2.7 Robustness to Observation Noise

Another question of interest is to study whether sparse reconstruction is robust in the presence of white Gaussian random observation noise. In other words, what would be the effect of observational noise on the image quality?

To answer these questions, I added white Gaussian random noise to the synthetic noise-free scattered data used in the fault model example with the dense acquisition geometry. The white Gaussian random noise distribution has a zero mean and a variance of γ^2 and about 68% of the noise lies within one standard deviation (STDV $= 1\gamma$) away from the mean.

I used the compressed-sensing algorithm to image different datasets with standard deviations γ equals to 5, 10, and 40. Given that the signal-to-noise ratio (SNR) is the average power of the signal divided by the average power of the noise, these datasets have signal-to-noise ratios of 9, 2.27, and 0.142, respectively. The migrated images for these different variances are shown in Figure 3.6.

In the case of the smallest standard deviation, the compressed-sensing solution in Figure 2.5(a) is quite similar to the compressed-sensing solution in the noise-free case shown in Figure 2.4(a). However, when the standard deviation is equal to 10, the solution plotted in Figure 2.5(b) tends to be smoother but it is not as heavily blurred as the noise-free least-square solution in Figure 2.3(d) and has more accurate amplitude information. The robustness of the compressed-sensing algorithm deteriorates dramatically as shown in Figure 2.5(c) when the average noise power is larger than the average power of the signal (SNR $\approx$ 0.142). This represents an extreme case where the forward modeling operator fails to explain the considerable amount of noise living in its null space.

2.8 Robustness to Velocity Error

Building an accurate velocity model and estimating the right velocity for migration is what makes the seismic imaging problem quite difficult. For this reason, I need to assess the robustness of the sparsely recovered solution in the presence of velocity error.

Therefore, I applied the compressed sensing migration to the recorded data using the dense acquisition geometry with velocity models that are 3% and 5% faster than the exact velocity model. The results are plotted in Figure 2.6(a) and Figure 2.6(b), respectively. The reflectors are fairly spatially focused in Figure 2.6(a) compared with the defocused events in Figure 2.6(b). Also, the two figures show that the fault plane is mispositioned and the reflectors, especially the deeper ones, are pushed down.

As expected, the reflectors, especially the deeper ones, are pulled up when using a 3% and 5% slower migration velocity to apply the compressed sensing migration as shown in Figure 2.6(c) and Figure 2.6(d), respectively.

Henceforth, compressed sensing based migration still retrieve fairly sparse migrated images even though the seismic events get defocused and mispositioned when the velocity error increases. Similarly, I obtain the least-square solutions using the erroneous velocities and these are shown in Figure 3.7 for comparison. Clearly, these solutions are strongly obscured by the migration smiles and the reflectors are considerably defocused compared with the CS solution.

2.9 Conclusions

Standard migration suffers from migration artifacts and low spatial resolution due to the limited aperture, coarse source-receiver sampling, band-limited nature of the source wavelet, and low subsurface illumination. These standard images obtained by applying the adjoint operator managed to retrieve a blurred depiction of the true subsurface reflectivity distribution.

Least-square migration algorithm helps suppress migration artifacts and enhance the spatial resolution of the migrated section by iteratively finding a subsurface reflectivity model that explains the observed data in a least-square sense. However, its solution might still be smooth whereas the subsurface reflectivity distribution is inherently sparse.

Formulating the Kirchhoff modeling-migration problem as a Basis Pursuit denoise problem is proven to be quite useful. Solving the Basis Pursuit denoise problem managed to recover a sparse subsurface reflectivity model that explains the data with more accurate amplitude information.

The compressed-sensing algorithm was tested on different subsurface models and it showed that compressed-sensing solutions significantly reduce the migration artifacts, enhance the spatial resolution, and recover more accurate amplitudes of the reflectors and scatterers than the smooth least-square solutions. The compressed-sensing algorithm dramatically compresses the smearing artifact caused by the adjoint operator and places much of the energy at corresponding subsurface point scatterer.

Also, by deploying only 20% of the available sources and receivers, compressed sensing migration retrieves a fairly focused and accurate subsurface reflectivity model using a smaller number of measurements. This could potentially lead to huge savings in resources and computational time. I also demonstrated the robustness of compressed sensing in the presence of white Gaussian random noise. Overall, the compressed-sensing algorithm still retrieves a sparse reflectivity model if the noise variance is small. The quality of the image deteriorates and becomes smoothed and less sparse as I increase the noise variance resulting in migrated images that are comparable to the noise-free least-square solutions.

I also demonstrated that the compressed sensing migration is quite robust when using inaccurate migration velocities. Using compressed sensing migration, I was able to recover fairly sparse migrated images even though the seismic events become more defocused and mispositioned as I used more erroneous migration velocities.

I finally conclude that compressed sensing based migration provides an efficient algorithm to recover sparse representations of subsurface reflectivity distributions. Although one of its major limitations is the sensitivity to errors in migration velocity, it tends to promote sparsity in the solution. So, I would expect the CS solution to be more relevant than standard migration or LSM solutions if the true signal is sparse.

In future work, I will consider applying the CS based imaging to a real data example and also to a complex salt synthetic model using a reverse time migration (RTM) framework instead of Kirchhoff migration.

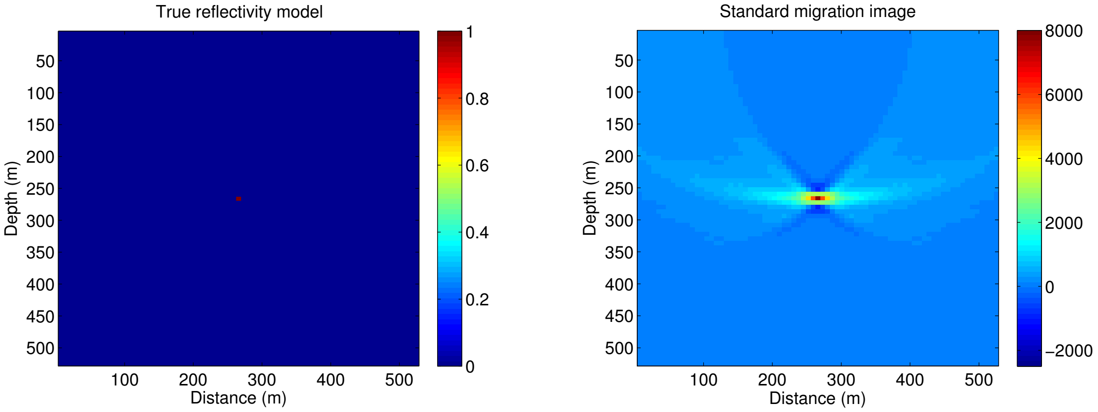

(a)) True reflectivity model (b)) Standard migration image

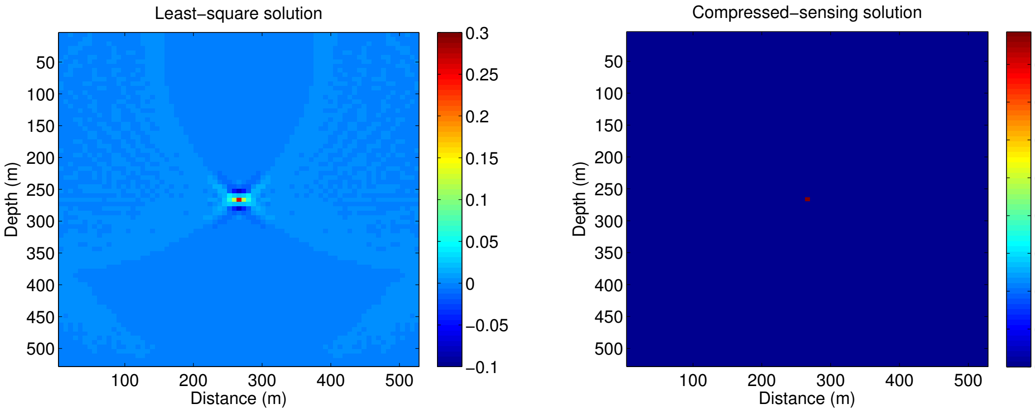

(c)) Least-square solution (d)) Compressed-sensing solution

Figure 2.1: Single scatterer example. a) True reflectivity model. b) Heavily blurred standard migrated image. c) Least-square migrated image suppresses the migration smiles but it results in a smooth depiction of the true reflectivity model. d) The compressed-sensing solution dramatically suppresses the migration smiles and give more accurate amplitude information of the scatterer.

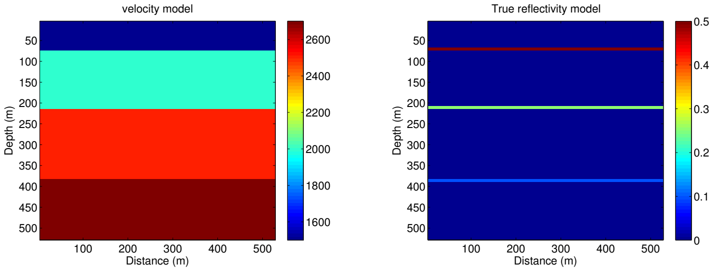

(a)) Velocity Model (b)) True reflectivity model

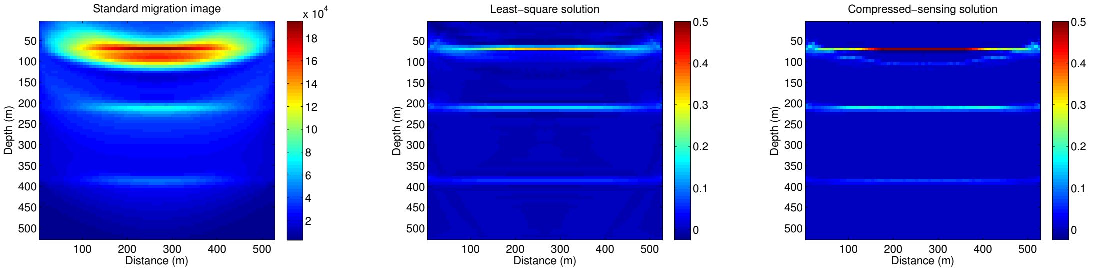

(c)) Standard migration image (d)) Least-square solution (e)) Compressed-sensing solution

Figure 2.2: Horizontal layers example. a) Velocity Model. b) True subsurface reflectivity distribution with three reflectors. c) Blurred standard migrated image. The reflectors are poorly resolved especially near the edges of the model. d) Least-square migration enhances the spatial resolution and suppresses the smearing artifacts but the energy of each reflector is smeared over neighboring depth samples. e) The compressed- sensing solution focuses the reflectors, suppresses the migration artifacts, and gives accurate amplitude information especially close to the higher coverage area.

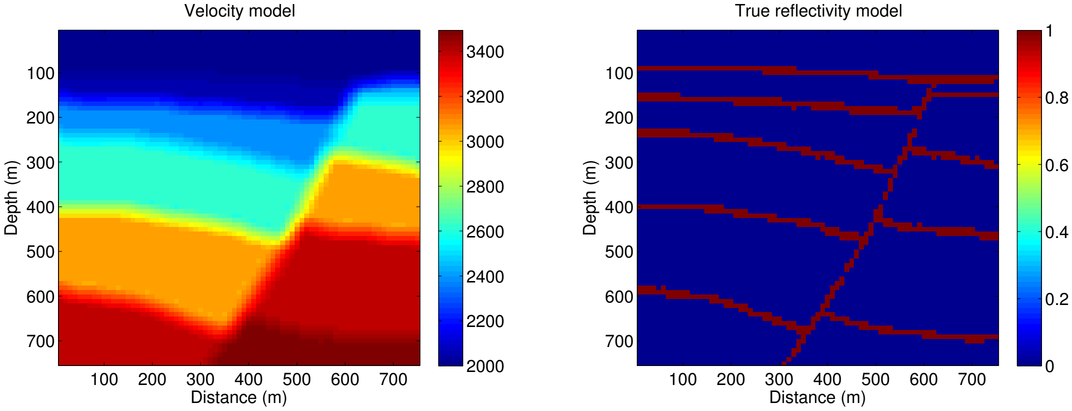

(a)) Velocity model
(b)) True reflectivity model

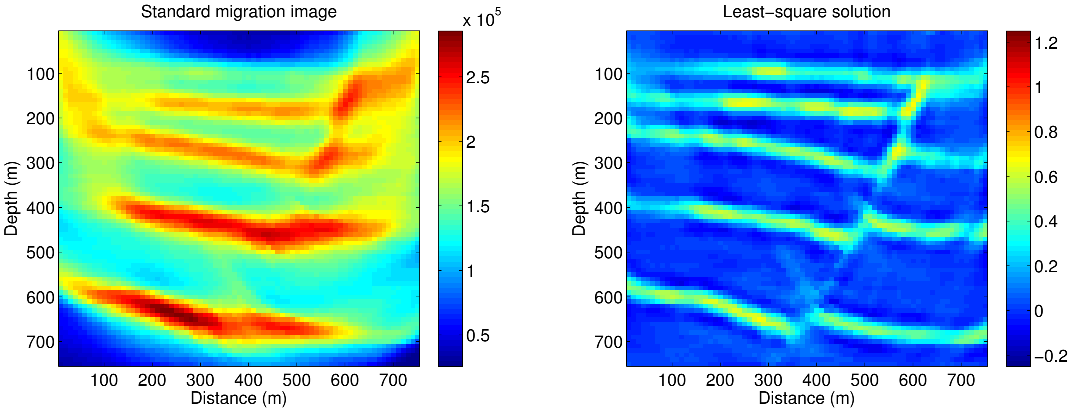

(c)) Standard migration image
(d)) Least-square solution

Figure 2.3: Fault model example. a) Smooth velocity model. b) True subsurface reflectivity distribution. c) Blurred standard migrated image. It is hard to delineate the fault plane accurately. d) Least-square migration enhances the spatial resolution and suppresses the smearing artifacts but still gives a smooth and dispersed version of the true reflectivity model.

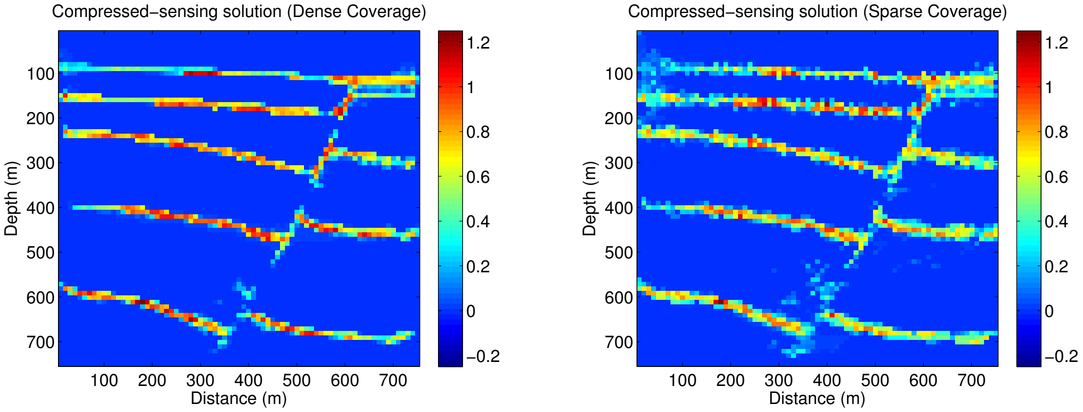

(a)) CS solution (dense coverage)

(b)) CS solution (sparse coverage)

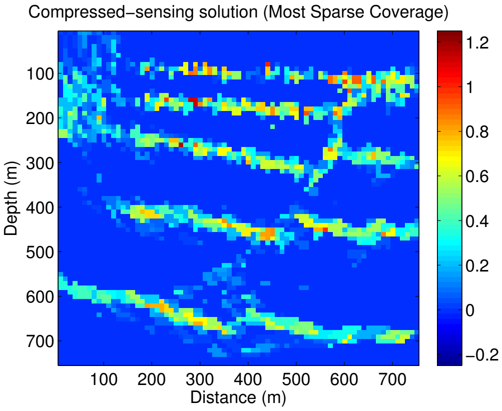

(c)) CS solution (very sparse coverage)

Figure 2.4: Fault model example. a) The compressed-sensing solution utilizing all 75 sources and receivers provides a highly focused migrated image with more accurate amplitude information. b) The compressed-sensing solution utilizing only 4% of the available sources and receivers gives a reasonably compressed and focused migrated image. c) The compressed-sensing solution with only 5 sources and 5 receivers shows the deterioration of the capability of the compressed-sensing migration to resolve the image.

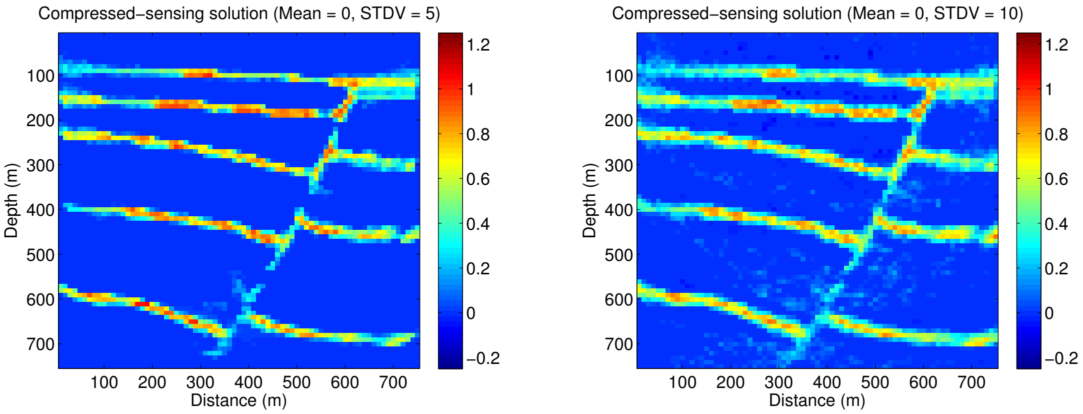

(a)) CS solution with $\gamma = 5$

(b)) CS solution with $\gamma = 10$

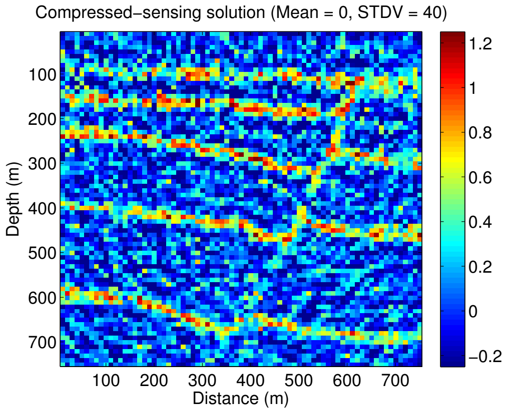

(c)) CS solution with $\gamma = 40$

Figure 2.5: The compressed-sensing solutions obtained from the noisy data after the addition of white Gaussian random noise with different standard deviations (STDV): a) $\gamma = 5$, b) $\gamma = 10$, and c) $\gamma = 40$.

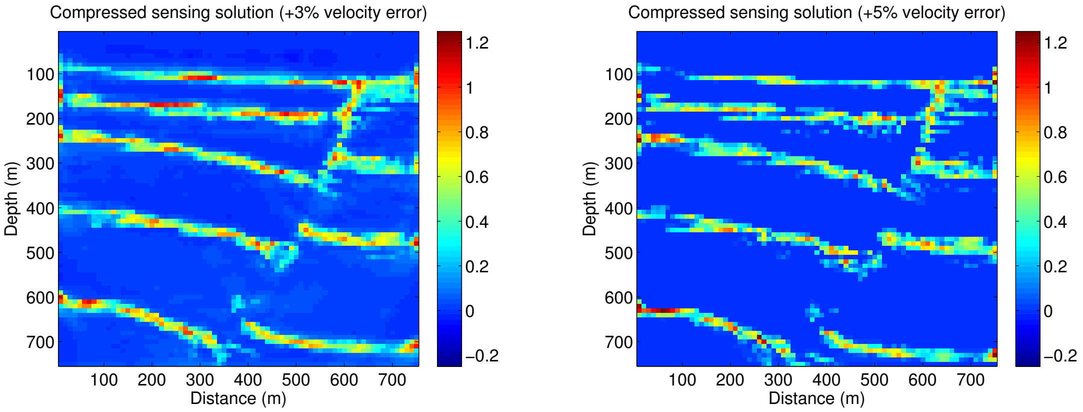

(a)) CS solution using a 3% faster velocity model (b)) CS solution using a 5% faster velocity model

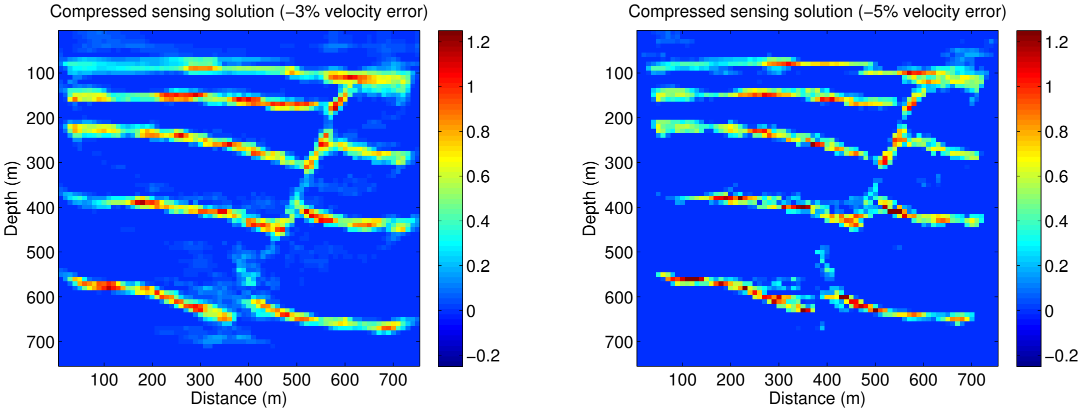

(c)) CS solution using a 3% slower velocity model (d)) CS solution using a 5% slower velocity model

Figure 2.6: The compressed-sensing images using inaccurate migration velocities : a) 3% faster velocity, b) 5% faster velocity, c) 3% slower velocity, and d) 5% slower velocity.

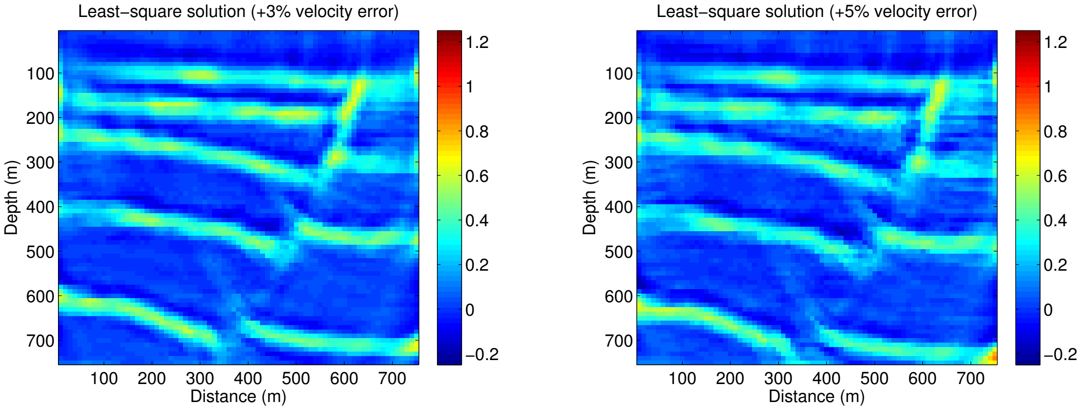

(a)) LSM solution using a 3% faster velocity model

(b)) LSM solution using a 5% faster velocity model

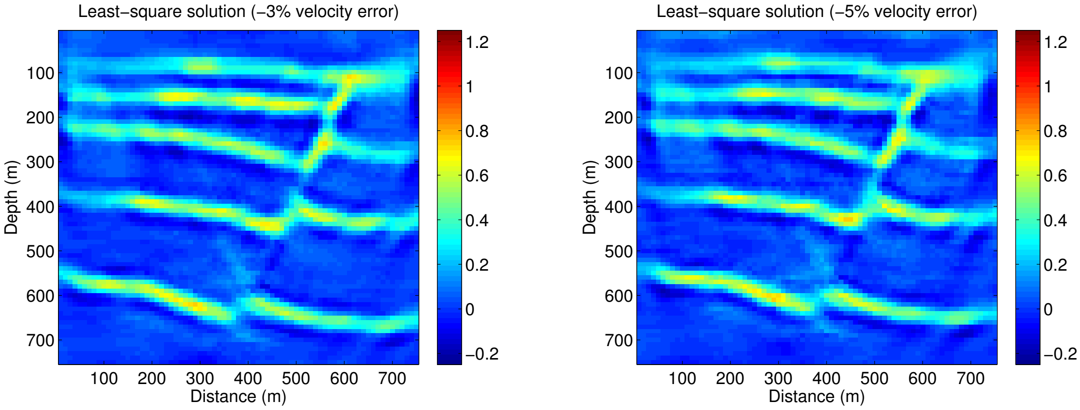

(c)) LSM solution using a 3% slower velocity model

(d)) LSM solution using a 5% slower velocity model

Figure 2.7: The least-square migrated images using inaccurate migration velocities : a) 3% faster velocity, b) 5% faster velocity, c) 3% slower velocity, and d) 5% slower velocity.

Chapter 3

The Possibilities of Least-squares Migration of Internally Scattered Seismic Energy

Approximate images of the Earth subsurface structures are usually obtained by migrating surface seismic data. Least-squares migration, under the single-scattering assumption, is utilized as an iterative linearized inversion scheme to suppress the migration artifacts, deconvolve the source signature, mitigate the acquisition fingerprint, and enhance the spatial resolution of migrated images. The problem with the least-squares migration of primaries, however, is that it may not be able to enhance events that are mainly illuminated by internal multiples, such as vertical and nearly vertical faults, or salt flanks. To alleviate this problem, I propose a linearized inversion framework to migrate internally scattered energy. I apply the least-squares migration of first-order internal multiples to image subsurface vertical fault planes. Tests on synthetic data demonstrate the ability of the proposed method to resolve vertical fault planes, which are poorly illuminated by the least-squares migration of primaries only. I, also, demonstrate the robustness of the proposed scheme in the presence of white Gaussian observational noise and in the case of imaging the fault planes using inaccurate migration velocities. The results suggest that the proposed least-squares imaging, under the double-scattering assumption, still retrieves the vertical fault planes when imaging the scattered data despite a slight defocusing of these events due to the presence of noise or velocity errors.

3.1 Introduction

Seismic imaging using Kirchhoff-type integrals, based on the high frequency asymptotic solution to the wave-equation, is a powerful tool to map the data recorded on the surface of the Earth into representative subsurface structures (Claerbout, 1992). However, a major drawback of standard Kirchhoff migration is that it mainly images reflectors that are primarily illuminated by single-scattering energy. In other words, it focuses the seismic energy that travels from a source point and bounces only once off a subsurface scattering point before it is received at a surface receiver. The reason is that the recording surface in seismic acquisition surveys does not typically enclose the medium containing the scattering points. Therefore, in the case of a complex velocity structure, some seismic energy may bounce once off a subsurface scattering point without ending up at the recording surface (Zuberi and Alkhalifah, 2014a). Figure 1a shows schematically a reflected ray that does not reach a recording station after a single reflection, pointing away from the recording surface.

Imaging internal multiples has the potential to retrieve seismic events that are poorly illuminated by single-scattering energy, such as vertical and nearly vertical fault planes, or salt flanks (Aldawood et al., 2014b). Internally scattered seismic energy may have a path that could end up on the recording surface allowing the illumination of such reflectors. Figure 1b shows schematically a doubly-reflected ray with a raypath that ends up on the recording surface. Malcolm et al. (2009) proposed a methodology to image internal multiples, in which they image prismatic waves and other higher order internal multiples. Behura et al. (2012) proposed an iterative imaging procedure to image internal scattering along with single scattering energy. Their methodology is based on virtual source creation using inverse scattering (Wapenaar et al., 2012). Zuberi and Alkhalifah (2013) proposed a three-step interferometric imaging procedure to image first-order internal scattering energy. Recently, Zuberi and Alkhalifah (2014a) generalized their interferometric technique to include higher order internal multiples. Their generalized interferometric multiple imaging procedure simultaneously creates and images internal multiples given that they are kinematically allowed to be in the recorded data.

Standard Kirchhoff-based, or RTM-based imaging is performed by applying the corresponding adjoint of the forward modeling operators to the single-scattered surface seismic data and correlating it with the forward modeled source wavefield to predict the location of the single scattering energy. Standard migration suffers from migration artifacts, which results in a blurred depiction of the true subsurface reflectivity distributions. This effect is primarily caused by the limited acquisition aperture, coarse source-receiver sampling, band-limited nature of the source wavelet, and low subsurface illumination (Nemeth et al., 1999; Tang, 2009). To remedy this problem, least-squares migration can be utilized to enhance the quality of migrated images and suppress the migration artifacts when imaging primaries, and to properly deconvolve the source wavelet and acquisition fingerprint (LeBras and Clayton, 1988; Nemeth et al., 1999). LSM provides an approximate solution for the subsurface reflectivity as demonstrated by the linearized waveform inversion (Snieder et al.; Landa et al., 1989; Crase et al., 1990; Roth and Tarantola). Dai et al. (2012) adapted the least-squares migration to image blended data in a multi-source RTM framework. Wang and Sacchi (2007), Herrmann and Li (2012), and Aldawood et al. (2014a) improved the least-squares imaging by imposing sparseness constraints on the least-squares solution to enhance the spatial resolution of the seismic events.

In this chapter, I extend the theory of least-squares migration to include the imaging of multiply-scattered seismic energy. I, first, describe how I linearize the problem of imaging internal multiples. Then, I apply the proposed linearized inversion to delineate synthetic vertical fault planes that are generally poorly illuminated by primaries. I, finally, demonstrate the robustness of the proposed linearized inversion framework to image these fault planes in the presence of white Gaussian observational noise and in the case of imaging the subsurface using erroneous migration velocities.

3.2 Single-scattering modeling and inversion

The Kirchhoff forward modeling operator **L** is a linear operator that maps the subsurface reflectivity distribution to single-scattered seismic data. Mathematically, generating synthetic seismic data corresponding to a reflectivity model of the Earth, $m(x)$, is obtained using the following forward modeling operator in the frequency domain:

$$d(s,g,\omega) = \int_V m(x)W(\omega)e^{i\omega(\tau_{sx}+\tau_{xg})}dx, \tag{3.1}$$

where $d(s,g,\omega)$ is the modeled single-scattered seismic data recorded at a surface receiver g due to a surface source located at s for a particular frequency ω. A point in the subsurface volume V is given by x, and $W(\omega)$ denotes the source wavelet. In addition, τ_{sx} is the travel time from the source point s to the subsurface scattering point x and τ_{xg} is the travel time from the subsurface scattering point x to the receiver point g. In a matrix form, the modeling can be represented by the following matrix-vector multiplication:

$$\mathbf{d} = \mathbf{L}\mathbf{m}, \tag{3.2}$$

where **d** is the recorded single-scattered data vector, and **m** is the subsurface reflectivity vector. A standard migrated image is obtained by applying the adjoint of the forward modeling operator $\mathbf{L^T}$ to the single-scattered seismic data (Claerbout, 1992). The adjoint operator linearly maps the single-scattered seismic data to subsurface structures of the Earth as follows:

$$m_{mig}(x) = \int_s \int_g \int_\omega d(s, g, \omega) W^*(\omega) e^{-i\omega(\tau_{sx}+\tau_{xg})} ds\ dg\ d\omega, \tag{3.3}$$

where $m_{mig}(x)$ is the standard migrated image and $W^*(\omega)$ is the complex conjugate of the source wavelet. While the integration is over the model space x for modeling seismic data, it is over the data space s, g, and ω for imaging recorded data. Physically, the single-scattered data $d(s, g, \omega)$ is back propagated from the receiver point g to the trial imaging point at x and the source function is forward propagated from the source point s to the trial imaging point at x. Then, the image value at the trial imaging point x is given by the zero-lag cross correlation between the forward and backward propagated wavefields, which is obtained by the summation over frequencies in equation (3.3). In a matrix representation, the Kirchhoff migration is given by a matrix-vector multiplication as follows:

$$\mathbf{m_{mig}} = \mathbf{L^T d}. \tag{3.4}$$

The migration operators are adjoint operators of the forward modeling ones as they *undo* the time and phase shifts of the modeling operators but do not account for the amplitude (Claerbout and Fomel, 2008). Substituting the expression of $\mathbf{d}$ in equation (3.2) into equation (3.4) yields:

$$\mathbf{m_{mig}} = \mathbf{L^T L m}, \tag{3.5}$$

where $\mathbf{L^T L}$ is known as the Hessian matrix and reflects the amount of smearing in the seismic image resulting from many factors, including the limited recording aperture, the coarse source-receiver samplings, and the band-limited nature of the source wavelet. The standard migrated image is, therefore, a linear combination of the columns of the Hessian matrix weighted by the true reflectivity model (Aster et al., 2005), providing a physical interpretation of the model resolution.

Least-squares migration yields an approximate reflectivity image that minimizes the sum of the squares of the residual vector. Mathematically, the unconstrained objective function is defined as:

$$J = \frac{1}{2}\|\mathbf{Lm} - \mathbf{d}\|_2^2 = \mathbf{\frac{1}{2}}\mathbf{m^T L^T L m} - \mathbf{m^T L^T d} + \mathbf{\frac{1}{2}}\mathbf{d^T d}. \tag{3.6}$$

The minimizer of this objective function is found by computing the gradient with respect to $\mathbf{m}$ and setting it to zero:

$$\nabla_{\mathbf{m}} J = \mathbf{L^T L m} - \mathbf{L^T d} = 0. \tag{3.7}$$

A more accurate solution to the migration problem is the least-squares migrated image $\mathbf{m_{ls}}$, which obtained by solving equation (3.7), the so-called normal equation:

$$\mathbf{L^T L m_{ls}} = \mathbf{L^T d}. \tag{3.8}$$

Gradient-based algorithms are generally used to solve this equation iteratively where data residuals are imaged at every iteration to obtain model updates. By re-arranging the terms in equation (3.7), the gradient at every iteration is given by:

$$\nabla_{\mathbf{m}} J = \mathbf{L^T}(\mathbf{Lm} - \mathbf{d}) = \mathbf{L^T r}, \tag{3.9}$$

where $\mathbf{r}$ is the data residual vector. An initial guess is usually given by the image resulting from the standard Kirchhoff migration in equation (3.3). At each iteration, the forward modeling operator in equation (3.1) is used to synthesize single-scattered seismic data to be compared with the recorded data. Then, the data residual is back-projected using the adjoint operator in equation (3.3) to determine the subsurface reflectivity model updates.

The least-squares migration, under the single-scattering assumption, suppresses the migration artifacts and enhances the seismic reflectors, which are mainly illuminated by primaries (Nemeth et al., 1999). However, it hardly delineates reflectors that are mainly illuminated by internally-scattered energy (Aldawood et al., 2014b). Consequently, imaging internal multiples potentially helps illuminate subsurface areas that are poorly illuminated by primaries, such as vertical and nearly vertical fault planes (Zuberi and Alkhalifah, 2013).

3.3 Double-scattering modeling and inversion

The following forward modeling operator maps the reflectivity model to doubly-scattered seismic data as:

$$d_d(s,g,\omega) = \int_V \int_V v(x)v(x')W(\omega)e^{i\omega(\tau_{sx}+\tau_{xx'}+\tau_{x'g})}dx\, dx', \tag{3.10}$$

where $d_d(s,g,\omega)$ is the recorded doubly-scattered seismic data. $v(x)$ and $v(x')$ are the subsurface reflectivity functions at subsurface points x and x', respectively. In addition, τ_{sx} is the travel time from the source point s to the first scattering point x. $\tau_{xx'}$ is the travel time from the first scattering point x to the second scattering point x'. Similarly, $\tau_{x'g}$ is the travel time from the second scattering point x' to the receiver point g.

Clearly, equation (3.10) shows that generating first-order internal multiples is not simply obtained by a linear mapping of the subsurface reflectivity model because of the multiplication of two reflectivity functions inside this double-summation modeling step. To linearize this operator, I propose replacing $v(x')$ by the fixed least-squares migration solution $p(x')$ under the single-scattering assumption, obtained by iteratively solving the normal equation (5.6). Equation (3.10) then becomes:

$$d_d(s, g, \omega) = \int_V \int_V v(x) p(x') W(\omega) e^{i\omega(\tau_{sx} + \tau_{xx'} + \tau_{x'g})} dx \, dx'. \tag{3.11}$$

Physically, the scattering points in the least-squares image $p(x)$ under the single-scattering assumption act as secondary sources to predict the doubly-scattered internal multiples. To predict a first-order internal multiple, the seismic energy is forward propagated from the source point s to the known scattering point x' and scaled by its reflectivity value $p(x')$. Then, the energy is emitted from this secondary source at x' and forward propagated to the second scattering point x and scaled by its reflectivity value $v(x)$. Lastly, the energy is further propagated from the second scattering point to the receiver point g to predict the internally scattered first-order multiple. In a similar approach, Zhang and Duan (2012) used the RTM reflectivity image as a secondary source in the subsurface to predict both interbed and surface-related multiples in their reverse time demigration (RTDM) framework.

The proposed prediction step of first-order multiples can then be represented by the following matrix-vector multiplication:

$$\mathbf{d_d} = \mathbf{G}\mathbf{v}, \tag{3.12}$$

where $\mathbf{G}$ is the forward modeling operator that linearly maps the subsurface reflectivity distribution, which is mainly illuminated by the doubly-scattered energy $\mathbf{v}$, to first-order internal multiples $\mathbf{d_d}$. The corresponding adjoint of this forward modeling operator can be applied to image the doubly-scattered data as follows:

$$v_{mig}(x) = \int_s \int_g \int_\omega \int_V d_d(s, g, \omega) p(x') W(\omega) e^{-i\omega(\tau_{sx} + \tau_{xx'} + \tau_{x'g})} ds \, dg \, d\omega \, dx'. \tag{3.13}$$

The physical interpretation of this equation is that the subsurface reflectivity image, under the double-scattering assumption, can be obtained by applying the following steps:

1. The doubly-scattered seismic data is back propagated from the receiver point g to the known scattering point x' and the seismic energy is scaled by the known reflectivity value $p(x')$ at this subsurface scattering point.
2. The scaled redatumed data at the known scattering point x' is further back propagated to the trial imaging point x.
3. The source wavefield is forward propagated from the source point s to the trial imaging point x.
4. I obtain the final image at the trial subsurface scattering point x by applying the zero-lag imaging condition of both the forward and backward propagated wavefields.

In a matrix form, the subsurface image, under the double-scattering assumption, $\mathbf{v_{mig}}$, is obtained by applying the adjoint operator $\mathbf{G^T}$ to the first-order internal multiples $\mathbf{d_d}$:

$$\mathbf{v_{mig}} = \mathbf{G^T d_d}. \tag{3.14}$$

Similarly to the single-scattering case, computing the doubly-scattered migrated image is determined by a linear mapping of the doubly-scattered seismic data. One can also solve a corresponding normal equation iteratively in order to obtain a least-squares migrated image $\mathbf{v_{ls}}$ under the double-scattering assumption as follows:

$$\mathbf{G^T G v_{ls}} = \mathbf{G^T d_d}. \tag{3.15}$$

The least-squares migration of both the single-scattering and double-scattering energy helps suppress the migration artifacts, remove the acquisition footprint, and deconvolve the source wavelet. It further enhances the spatial resolution of both horizontal reflectors and vertical fault planes. Equations (5.6) and (3.15) are usually solved iteratively using a gradient-based optimization algorithm. Here, I use the limited memeory BFGS (L-BFGS) optimization algorithm to obtain the least-squares solutions. See Appendix A for a more detailed description of the algorithm.

3.4 Imaging vertical fault planes

In the following two examples, the grid spacings of the 100 by 50 grids are $\Delta x = \Delta z = 30$ meters, and the time sampling is 4 ms. I computed 100 noise-free common shot gathers along the surface using the forward modeling operators to generate the primaries and first-order internal multiples. A Ricker wavelet with a peak frequency of 20 Hz was used to model the seismic data. The first shot is at the top-left corner and the last shot is at the top-right corner. The remaining equally spaced shots are placed at the grid points along the Earth surface. Similarly, there are 100 equally spaced receivers placed at the grid points along the Earth surface.

The first velocity and reflectivity models are shown in Figure 2a and Figure 2b, respectively. In this example, the two-layer velocity is given by 2500 m/s and 3000 m/s from top to bottom and the CDP sampling is 15 m. The dominant frequency of 20 Hz results in a dominant wavelength of 125 to 150 meters. Thus, the image point is sufficiently sampled at about 8-10 points per wavelength. On the other hand, the second velocity and reflectivity models are shown in Figure 3a and Figure 3b, respectively. In this case, the velocity ranges between 1500 m/s and 3900 m/s and the CDP sampling is 15 meters. Using the same Ricker wavelet, the dominant wavelength ranges from 75 to 195 meters. Hence, the image point is sampled sufficiently at 5-13 point per wavelength. The goal is to apply the proposed least-squares migration of first-order internal multiples to properly image the vertical fault planes in these two different models.

The images obtained using the standard migration of the noise-free data, under the single-scattering assumption, are shown in Figure 4a and Figure 4b, respectively. The figures show blurry depictions of the true subsurface reflectivity distributions due to the migration artifacts, the acquisition fingerprint, and the limited bandwidth of the source wavelet. To alleviate these problems, the least-squares migration, under the single-scattering assumption, is applied to suppress the migration artifacts and sharpen the reflectors as shown in Figure 5a and Figure 5b, respectively. After 30 quasi-Newton L-BFGS iterations, this linearized inversion mainly enhances the horizontal reflectors, which are mostly illuminated by primaries. The vertical fault planes, however, are not well delineated since they are mainly illuminated by internally scattered seismic energy.

The least-squares solutions in Figure 5a and Figure 5b, under the single-scattering assumption, are then used in equations (3.11) and (3.13) to linearize the inversion of the first-order internal multiples using the proposed framework. These solutions are further used as an initial guess to start the proposed linearized inversion. After 11 quasi-Newton L-BFGS iterations, the least-squares migration results, based on the double-scattering assumption, are shown in Figure 6a and Figure 6b, respectively. Clearly, inverting the first-order internal multiples delineates the fault planes and localizes them in their true subsurface positions.

3.5 Robustness to Observation Noise

A challenging question is to assess whether one can accurately delineate the vertical fault plane in the presence of white observational noise. To answer this question, I added white Gaussian random noise to the two synthetic noise-free datasets. I then used the proposed least-squares migration framework to image the first-order internal multiples in order to assess the robustness of this linearized inversion.

The least-squares images, under the double-scattering assumption, of the two noisy datasets with a signal-to-noise ratio of -15 dB and -10 dB are shown in Figure 7a and Figure 7b, respectively. These solutions, obtained after 10 quasi-Newton L-BFGS iterations, still show a clear delineation of the fault planes despite the defocusing of the seismic events. However, as the data becomes noisy, the quality of the LSM images, under the double-scattering assumption, deteriorates compared with the noise-free images shown in Figure 5a and Figure 5b.

3.6 Robustness to Velocity Error

Velocity model building to estimate accurate migration velocities is one of the major challenges in seismic imaging. Hence, another question of interest is to study whether the proposed linearized inversion of doubly-scattered data is robust in the case of imaging with inaccurate migration velocities. In other words, what is the effect of velocity errors on the final image quality, and on the ability of the proposed framework to resolve the vertical fault planes?

To answer these questions, I applied the linearized framework to image first-order internal multiples using slower and faster migration velocities. I first compute the least-squares solutions, under the single-scattering assumption, to image the recorded data with velocity models that are 1% faster and slower than the exact velocity model. The LSM solutions of the first and second examples, imaged using the slower and faster velocities, are plotted in Figures 8a and 8b, and in Figures 8c and 8d, respectively. One can see that these least-squares images become more defocused and mispositioned as the velocity becomes erroneous. Whereas the horizontal reflectors are pulled up when migrating the data using slower migration velocities, they are pushed down when the recorded data is imaged with faster migration velocities.

These images are then used as constraints and initial guesses in the linearized inversion framework under the double-scattering assumption. The least-squares solutions, obtained by imaging first-order internal multiples using the slower and faster velocities, are plotted in Figure 9a and 9b for the first example, and in Figure 9c and 9d for the second example. The vertical fault planes are fairly spatially focused in case the migration velocity error is ± 1% as demonstrated in these figures.

The results suggest that the proposed least-squares imaging, under the double-scattering assumption, can be sensitive to the accuracy of the migration velocity model and the accuracy of the scatterers' locations obtained by inverting the primaries. As a result, these two factors could cause more defocusing and mis-positioning of the vertical fault planes compared with the horizontal reflectors, which are mainly delineated by the least-squares migration of primaries.

3.7 Discussion

Standard migration suffers from migration artifacts and low spatial resolution due to the limited acquisition aperture, coarse source-receiver sampling, limited bandwidth of the source wavelet, and low subsurface illumination as shown in Figure 4. Least-squares migration helps suppress migration artifacts, remove the acquisition fingerprint, and enhance the spatial resolution of the migrated section by iteratively finding a subsurface reflectivity model that better explains the observed data in a least-squares sense.

However, both standard and iterative least-squares migration algorithms, under the single-scattering assumption, yield migrated sections that focus seismic events, which are mainly illuminated by primaries, such as horizontal reflectors as seen in Figures 4 and 5, respectively. I demonstrated that modeling doubly-scattered data is mathematically not represented by a linear mapping of the subsurface reflectivity distribution. Thus, I proposed a linearization step where I use the least-squares image, under the single-scattering assumption, as a constraint in the forward modeling and adjoint operators, which models and images first-order multiples, respectively. I, then, demonstrated the effectiveness of the proposed linearized inversion scheme of doubly-scattered energy and its ability to localize vertical fault planes in Figure 6.

I, also, demonstrated the robustness of this inversion framework in the presence of white Gaussian random observational noise. Overall, the proposed least-squares imaging, under the double-scattering assumption, still retrieves the vertical fault planes when imaging the noisy datasets despite the slight defocusing of these events due to the presence of noise as illustrated in Figure 7.

I finally studied the robustness of the proposed linearized inversion when imaging the data with inaccurate migration velocities. In Figure 9, I showed how the least-squares migration of the doubly-scattered data could delineate the vertical fault planes although they become mispositioned and unfocused in the presence of velocity errors. I conclude that the linearized inversion of first-order internal multiples can be sensitive to the migration velocity models and the constraining least-squares images of primaries.

3.8 Conclusions

I proposed a linearized inversion framework to invert first-order internal multiples in the seismic records. The least-square image, based on the single-scattering assumption, was used as a constraint to linearize the forward modeling and adjoint operators of doubly-scattered energy. The results on synthetic data revealed the effectiveness of the proposed linearized inversion in delineating vertical fault planes, which are mainly illuminated by doubly-scattered seismic energy. I further demonstrated the robustness of the least-squares migration of first-order multiples in the presence of noise and in case of imaging using inaccurate velocities. In conclusion, I would expect the proposed least-squares migration, under the double-scattering assumption, to work best in case the data quality is high, and both the single-scattered least-squares image and the migration velocity model are quite accurate.

Future work will consider employing a sparsity-promoting imaging framework to obtain highly focused images with the proposed linearized inversion. It will also include the application of this least-squares imaging technique to real data examples and 3D synthetic models in an efficient RTM framework instead of the currently used Kirchhoff-based framework.

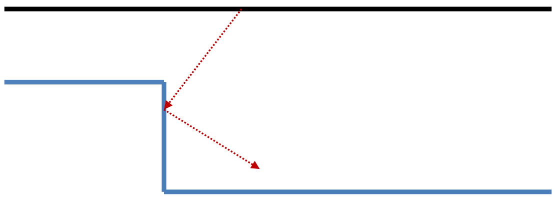

(a) Singly-reflected ray

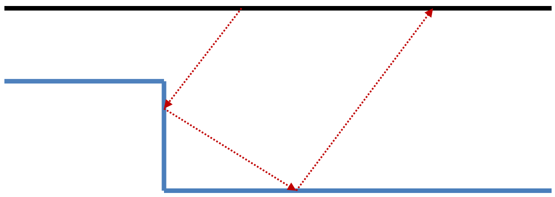

(b) Doubly-reflected ray

Figure 3.1: Ray diagrams: a) A singly-scattered ray is reflected off the vertical fault plane away from the recording surface. b) A doubly-reflected ray ends up at the recording surface illuminating the vertical fault plane.

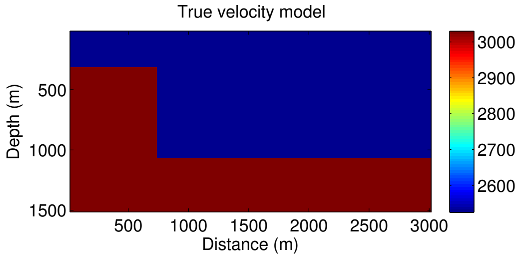

(a) True velocity model

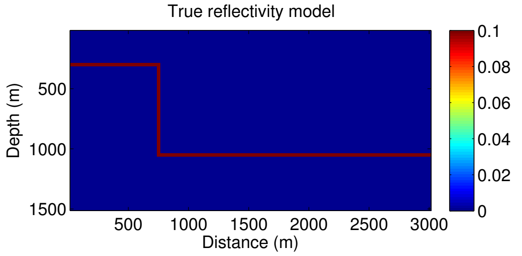

(b) True reflectivity model

Figure 3.2: A vertical fault plane: a) True velocity model. b) True reflectivity model.

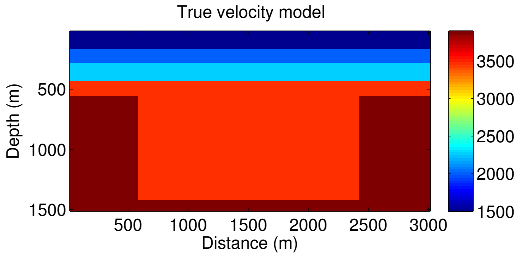

(a) True velocity model

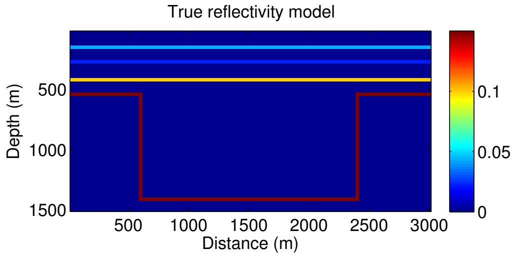

(b) True reflectivity model

Figure 3.3: Buried vertical faults: a) True velocity model. b) True reflectivity model.

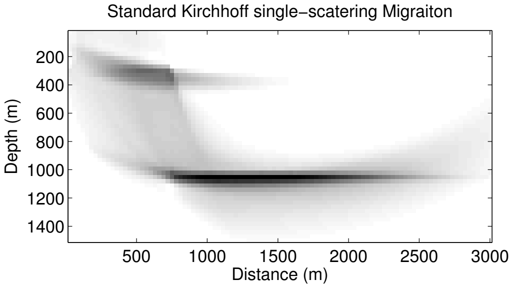

(a) Example 1: Kirchhoff migration

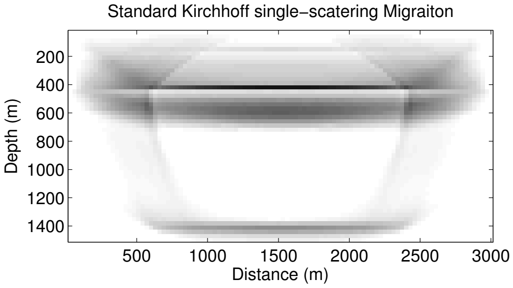

(b) Example 2: Kirchhoff migration

Figure 3.4: Standard Kirchhoff migration: a) Example 1: Kirchhoff migration of the two-layer model. b) Example 2: Kirchhoff migration of the buried vertical faults model. The standard Kirchhoff imaging of primaries only yields a blurry representation of the subsurface structures.

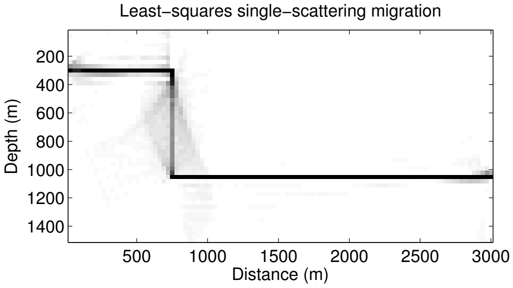

(a) Example 1: Single-scattering least-squares migration

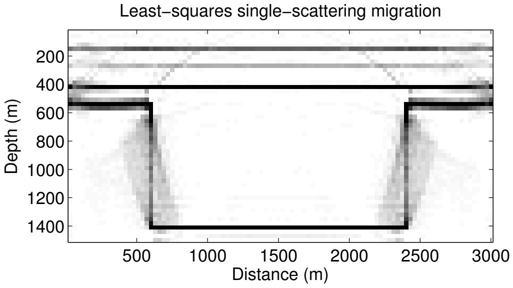

(b) Example 2: Single-scattering least-squares migration

Figure 3.5: Imaging vertical faults: a) Example 1: Single-scattering least-squares migrated image. b) Example 2: Single-scattering least-squares migrated image. The LSM of primaries only better emphasizes the horizontal reflectors.

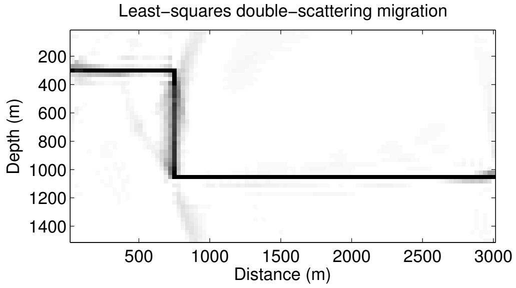

(a) Example 1: Double-scattering least-squares migration

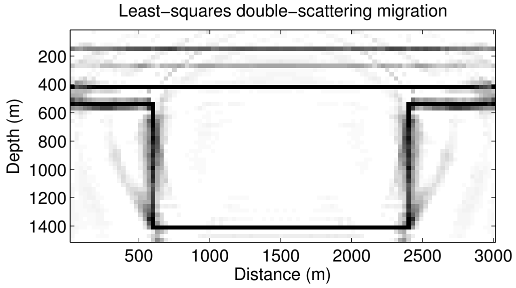

(b) Example 2: Double-scattering least-squares migration

Figure 3.6: Imaging vertical faults: a) Example 1: Double-scattering least-squares migrated image. b) Example 2: Double-scattering least-squares migrated image. The LSM of first-order internal multiples better delineates the vertical fault plane.

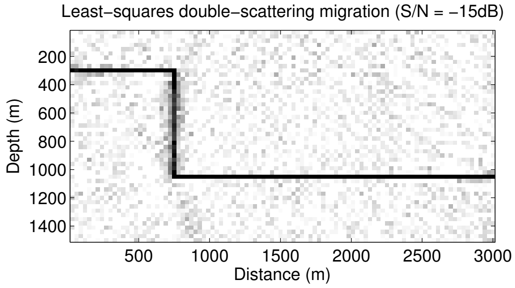

(a) Example 1: The LSM solution under the double-scattering assumption with SNR = -15 dB

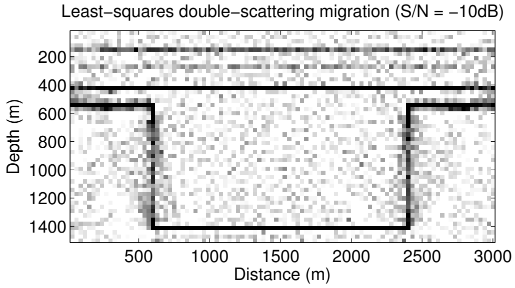

(b) Example 2: The LSM solution under the double-scattering assumption with SNR = -10 dB

Figure 3.7: Double-scattering least-squares migration of noisy datasets: a) Example 1: double-scattering LSM with SNR = -15 dB. b) Example 2: double-scattering LSM with SNR = -10 dB. As the data becomes noisy, the ability of the least-squares imaging of first-order internal multiples to delineate the vertical fault planes deteriorates.

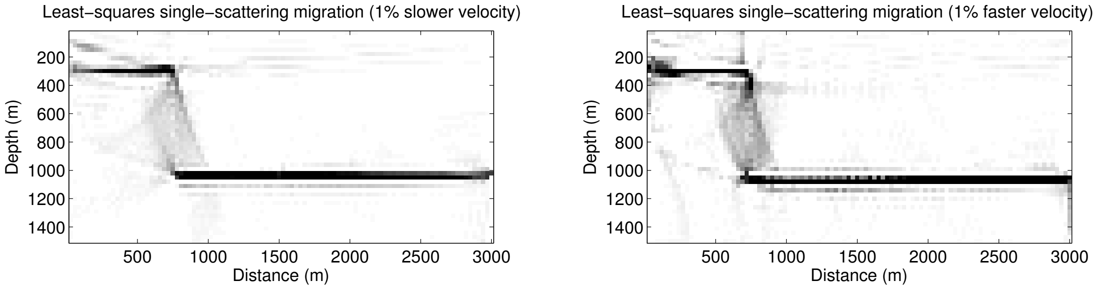

(a) Example 1: Single-scattering LSM using 1% slower velocity model

(b) Example 1: Single-scattering LSM using 1% faster velocity model

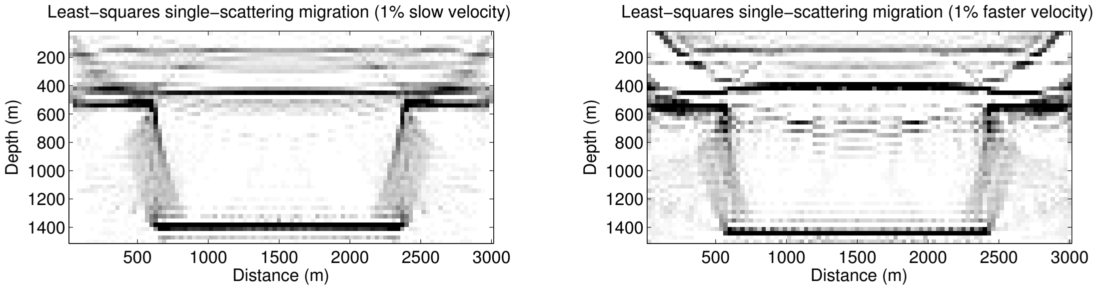

(c) Example 2: Single-scattering LSM using 1% slower velocity model

(d) Example 2: Single-scattering LSM using 1% faster velocity model

Figure 3.8: The LSM of primaries using the slower and faster migration velocities. Example 1: Least-squares migration using: a) 1% slower velocity model. b) 1% faster velocity model. Example 2: Least-squares migration using: c) 1% slower velocity. d) 1% faster velocity.

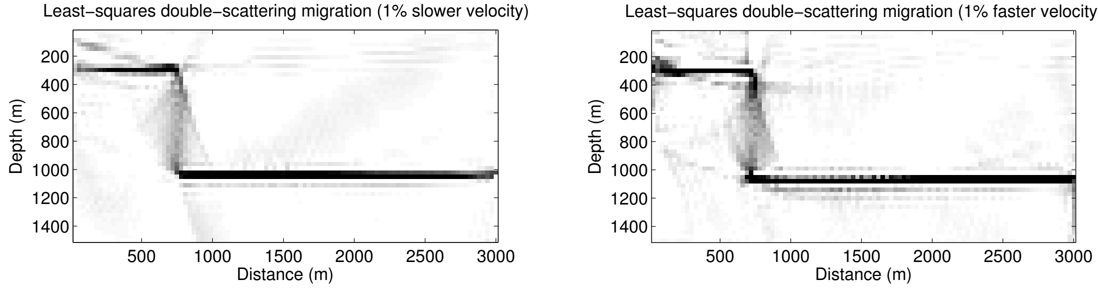

(a) Example 1: Double-scattering LSM using 1% slower velocity model

(b) Example 1: Double-scattering LSM using 1% faster velocity model

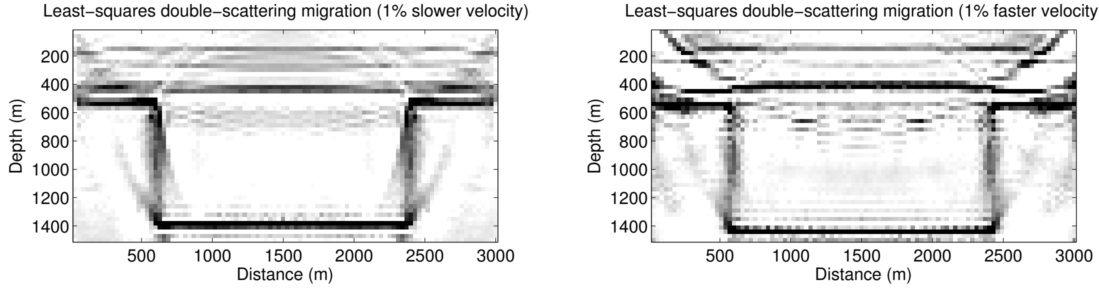

(c) Example 2: Double-scattering LSM using 1% slower velocity model

(d) Example 2: Double-scattering LSM using 1% faster velocity model

Figure 3.9: The LSM of first-order multiples using the slower and faster migration velocities. Example 1: Least-squares migration using: a) 1% slower velocity model. b) 1% faster velocity model. Example 2: Least-squares migration using: c) 1% slower velocity. d) 1% faster velocity.

Chapter 4

Least-squares Datuming of VSP Multiples

An approximate redatumed data is usually obtained by interferometric transformations, which can create virtual source or receiver positions. The conventional interferometric transformations are based on the cross-correlation or convolution of the recorded seismic traces. This redatuming of seismic data, however, suffers from low temporal resolution, wavelet distortion, and correlation artifacts due to the band-limited nature of the source wavelet, small number of sources and/or receivers in the acquisition geometry, limited recording aperture, and cross-correlation of the seismic traces. To alleviate these problems, I resort to the theory of least-squares datuming, which I apply to transform synthetic vertical-seismic-profile surface-related multiples into surface-seismic primaries. These primaries are subsequently imaged using a diffraction-stack migration formula to obtain subsurface structures. Numerical examples from a synthetic subsurface model demonstrates the effectiveness of the proposed least-squares datuming, showing clear enhancement in the quality and the frequency bandwidth of both the virtual surface-seismic gathers and the resolution of the final migrated section. I further modify both the datuming and modeling operators in the linearized inversion framework to include the transformation of vertical-seismic-profile internal multiples into surface-seismic primaries. The synthetic results show that the proposed operators help enhance the least-squares datumed events in both the virtual gathers and the migrated image.

4.1 Introduction

Seismic interferometry, also known as virtual source method, is widely used to transform recorded seismic data from one acquisition geometry to another. The power of interferometric transformations lies in their ability to redatum seismic data without knowing the underlying velocity model. Seismic interferometry basically requires the cross-correlations, or convolutions of the recorded seismic traces, which act as natural wavefield extrapolators (Wapenaar and Fokkema, 2006; Schuster, 2009). One may also use this approach to extract the impulse response between receivers by making suitable combinations of the wavefields recorded at these receivers from different sources (Snieder et al., 2006).

Vertical seismic profiling data are conventionally processed to enhance the upgoing primaries that are subsequently imaged to obtain subsurface structures whereas the downgoing multiples are suppressed or removed. Jiang and Hornby (2007) proposed a 3D data-driven method to predict VSP multiples using a convolution-type transformation. They convolved surface-seismic profile data with VSP direct energy to predict VSP multiples. Ma et al. (2011) used the SRME technique by combining surface-seismic and VSP data in their prediction-subtraction approach to attenuate VSP surface-related multiples. He et al. (2006) transformed the VSP multiples to surface seismic primaries by a VSP-SSP cross-correlation transform and imaged them using a 3D wave-equation migration. Wang et al. (2010) proposed a joint interferometric imaging workflow in which they use both primary and ghost reflections to image subsurface structures. Lu et al. (2006) used seismic interferometry to redatum surface sources into virtual sources in a vertical well to obtain a virtual dataset that mimics the response of down-hole sources and down-hole receivers. Then, they imaged these virtual traces using a targeted RTM step to delineate upward dipping salt-flank sedimentary layers.

However, interferometric transformation of seismic data, based on the cross-correlations of seismic traces, deteriorates the quality of the final migrated image. In other words, the image suffers from low spatial resolution due to the coarse source-receiver samplings, the limited acquisition aperture, and the distortion of the source wavelet, and the cross talk noise caused by the cross-correlation step. To alleviate these problems, Xue and Schuster (2008) proposed a least-squares datuming framework to suppress the datuming artifacts and enhance the quality of the redatumed gathers. In their Least-squares datuming, they proposed an iterative combined correlation-convolution workflow in which the cross-correlation of the traces acts as a linear datuming (adjoint) operator and the convolution of the traces acts as a linear de-datuming (forward modeling) linear operator to transform seismic data from one acquisition geometry to another. At every iteration, the adjoint (datuming) operator is applied to the forward modeled data residual in order to obtain the gradient, which could be used to the desired datumed dataset. In refraction seismology, Bharadwaj et al. (2012) and Alshuhail et al. (2012) used a cross-correlation datuming step followed by a convolution de-datuming step to enhance the first arrivals in their super-virtual refraction interferometry method. Recently, Al-Hagan et al. (2014) expanded the super-virtual refraction method and applied it using an iterative procedure to further enhance the first breaks by a combined correlation-convolution framework. Aldawood et al. (2015) compared and analyzed the different effects of applying least-squares migration and least-squares datuming when imaging VSP multiples.

In this chapter, I study the possibility of applying least-squares datuming to transform VSP surface-related multiples into virtual SSP data prior to imaging the virtual SSP primaries using Kirchhoff migration. I start by presenting both the forward modeling de-datuming operator and the adjoint datuming operator, which are used to transform VSP surface-related multiples into SSP primaries. I then migrate the LSD virtual SSP primaries using Kirchhoff-based imaging algorithm in order to obtain an approximate reflectivity image of the subsurface. I compare this image with the one obtained using the Kirchhoff migration of conventionally datumed SSP primaries based on cross-correlation interferometric transformation. I finally modify both the forward and adjoint operators to enable the datuming of internal VSP multiple in order to compute more accurate virtual SSP primaries in a least-squares sense and then migrate them to obtain an enhanced final image.

4.2 Least-squares datuming

The reciprocity equation of the correlation type can be used to linearly map the recorded VSP surface-related multiples to virtual SSP primaries. Mathematically, generating virtual datumed SSP primaries can be computed in the frequency domain using the following reciprocity equation (Wapenaar and Fokkema, 2006):

$$Im[G(B|A)] = k \int_{S_0} G_d(r|B)^* G(r|A) d^2 r, \tag{4.1}$$

where $G(B|A)$ represents a virtual SSP trace recorded at B due to a source at A. $G(r|A)$ is the recorded trace of VSP multiples at r due to a source at A. $G_d(r|B)^*$ is the complex conjugate of the recorded trace at r of the direct VSP energy due to a source at B. S_0 is the integration surface along the vertical well in the VSP acquisition geometry, and k is the wavenumber. A schematic ray diagram in Figure 4.1(a) shows that the cross-correlation of a VSP surface-related multiple with a VSP direct wave yields a virtual SSP primary, as the traveltime associated with the common ray path subtracts. Therefore, cross-correlating the VSP surface-related multiple event recorded at r due to a source at point A with the direct wavefield recorded at point

r due to a source at shot point B shifts the multiple event backward in time. This step yields a seismic event that represents the impulse response of a primary event recorded by a virtual receiver at point B due to a source at shot point A. In a matrix form, the above system in equation (4.1) can be represented by the following matrix-vector multiplication:

$$\mathbf{d}_{\mathbf{SSP}}^{\mathbf{virtual}} = \mathbf{J}^{\dagger}\mathbf{d}_{\mathbf{VSP}}, \tag{4.2}$$

where $\mathbf{J}^{\dagger}$ is the conventional cross-correlation adjoint operator (i.e. datuming operator), which linearly maps VSP surface-related multiples $\mathbf{d}_{\mathbf{VSP}}$ into virtual SSP primaries $\mathbf{d}_{\mathbf{SSP}}^{\mathbf{virtual}}$. The virtual SSP data $\mathbf{d}_{\mathbf{SSP}}^{\mathbf{virtual}}$ may suffer from wavelet distortion and low temporal resolution. It could also contain spurious seismic events known as correlation artifacts. These effects are caused by the imperfect summation in equation (4.1) due to the limited recording aperture along the vertical borehole, sparse sampling of the receivers in the well, and the cross-correlation of the seismic traces.

Least-squares datuming can be utilized to mitigate the cross-correlation artifacts, deconvolve the source wavelet, and enhance the resolution of the virtual SSP events (Xue and Schuster, 2008). LSD requires a forward modeling operator, which linearly transforms virtual SSP primaries into VSP surface-related multiples. In the frequency domain, the reciprocity equation of the convolution type can be implemented as a modeling operator as follows (Wapenaar and Fokkema, 2006):

$$G(r|A) = 2ik \int_{S_1} G_d(r|B)G(B|A)d^2B, \tag{4.3}$$

where the summation surface S_1 is now along the Earth surface over all "virtual" receiver positions B's. The reciprocity equation of the convolution type (4.3) undoes the phase and time shifts, which were applied to the VSP surface-related multiples by the reciprocity equation of the correlation type (4.1). The ray diagram in Figure

4.1(a) shows schematically that the convolution of a surface-seismic primary with a VSP direct wave yields a VSP surface-related multiple since the traveltimes add up. Therefore, convolving the virtual SSP primary event recorded at the virtual receiver at point B due to a source at point A with the direct wavefield recorded at r due to a source at point B shifts the primary event forward in time. This step yields a seismic event that represents the impulse response of a a VSP surface-related multiple event recorded by a receiver at point r due to a source at shot point A. In a matrix representation, equation (4.3) is given by the following matrix-vector multiplication:

$$\mathbf{d_{VSP}} = \mathbf{J}\mathbf{d_{SSP}^{virtual}}, \tag{4.4}$$

where the convolution type forward modeling operator $\mathbf{J}$ is applied to the virtual SSP primaries $\mathbf{d_{SSP}^{virtual}}$ to predict the VSP surface-related multiples $\mathbf{d_{VSP}}$. Therefore, the least-squares datumed SSP primaries $\mathbf{d_{SSP_{ls}}^{virtual}}$ are obtained by solving the following normal equation:

$$\mathbf{J}^{\dagger}\mathbf{J}\mathbf{d_{SSP_{ls}}^{virtual}} = \mathbf{J}^{\dagger}\mathbf{d_{VSP}}. \tag{4.5}$$

The linear system in equation (4.5) is solved iteratively using a gradient-based optimization algorithm. I used a quasi-Newton L-BFGS gradient-based method to invert the system in order to obtain the least-squares datumed SSP data after 30 iterations. See Appendix A for a more detailed description of the algorithm.

I also propose modified datuming and de-datuming operators that would convert VSP interbed multiples to SSP primaries. This can be achieved by replacing the trace containing the direct wavefield $G_d(r|B)$ by the full trace containing both the direct field and multiples $G(r|B)$ in the reciprocity equation of the correlation type (4.1) and the convolution type (4.3). The idea behind this modification is that the cross-correlation of a VSP internal multiple, which reflects off the free surface, with a lower order VSP internal multiple could create a virtual SSP primary.

Figure 5.1(b) shows schematically the capability of the modified datuming operator to transform a higher order VSP interbed multiple into an SSP primary by the cross-correlation of this higher order multiple with a lower order VSP interbed multiple. Therefore, cross-correlating the high-order VSP interbed multiple event recorded at r due to a source at shot point A with the lower-order VSP interbed multiple event recorded at point r due to a source at shot point B shifts the multiple event backward in time. This step yields a seismic event that represents the impulse response of a primary event recorded by a virtual receiver at B due to a source at shot point A.

Similarly, Figure 5.1(b) demonstrates schematically the ability of the modified forward modeling operator to predict a higher order VSP interbed multiple by convolving a lower order VSP interbed multiple with a virtual SSP primary. Hence, convolving the virtual SSP primary event recorded at the virtual receiver at point B due to a source at point A with a lower-order VSP interbed multiple recorded at r due to a source at B shifts the primary event forward in time. This step yields a seismic event that represents the impulse response of a a higher-order VSP interbed multiple event recorded by a receiver at point r due to a source at shot point A.

I then migrate the conventional cross-correlation datumed data $\mathbf{d}^{\mathbf{virtual}}_{\mathbf{SSP}}$ and the least-squares datumed data $\mathbf{d}^{\mathbf{virtual}}_{\mathbf{SSP_{ls}}}$ using Kirchhoff-type migration. The diffraction-stack migrated image is obtained by applying the following multidimensional summation in the frequency domain (Claerbout, 1992; Yilmaz, 2001)

$$m_{mig}(\mathbf{x}) = -\sum_{\mathbf{s}}\sum_{\mathbf{g}}\sum_{\omega}(i\omega)^2 d(\mathbf{s},\mathbf{g},\omega)e^{-i\omega(\tau_{\mathbf{sx}}+\tau_{\mathbf{xg}})}, \tag{4.6}$$

where $m_{mig}(\mathbf{x})$ is the diffraction stack migrated section, ω is the angular frequency, and $i = \sqrt{-1}$. $\tau_{\mathbf{sx}}$ is the traveltime from the surface source point $\mathbf{s}$ to the subsurface trial image point $\mathbf{x}$. Similarly, $\tau_{\mathbf{xg}}$ is the traveltime from the subsurface trial image point $\mathbf{x}$ to the surface receiver point $\mathbf{g}$. In this study, the surface-seismic data $d(\mathbf{s},\mathbf{g},\omega)$

is the virtual SSP data obtained by the conventional cross-correlation datuming or least-squares datuming.

4.3 Numerical Example

The true velocity model used to generate the synthetic VSP data is shown in Figure 4.3(a). In this 100 by 120 grid point model, the grid spacing is $\Delta x = \Delta z = 10$ m and the wavefield time sampling is 0.5 ms. The acquisition geometry consists of 100 shots equally spaced along the Earth surface and 16 receivers equally spaced from the depth range of 490 m to 790 m at the left side wall of the model. The source function is a Ricker wavelet with a dominant frequency of 25 Hz. I generated the VSP data using a finite-difference solution to the acoustic wave-equation. A typical common receiver gather is plotted in Figure 4.3(b).

I used the conventional correlation-type interferometric transformation in equation (4.1) to linearly transform VSP surface-related multiples into surface-seismic primaries. A datumed virtual SSP shot gather is plotted in Figure 4.4(a) and shows low temporal resolution, correlation artifacts, and wavelet distortion. These effects are due to the limited number of 16 receivers placed along a small aperture in the borehole resulting in an imperfect summation in equation (4.1). They are also caused by the cross-correlation process that does not properly deconvolve the source signature.

To remedy these problem, I iteratively solve the linear system in equation (4.5) to obtain the least-squared datumed virtual SSP gathers. The same virtual shot gather is plotted in Figure 4.4(b) after LSD for comparison. The figure shows that this linearized inversion yields a remarkable enhancement of the temporal resolution of the seismic events, the suppression of the correlation artifacts, and the deconvolution of the source wavelet. For comparison, Figures 4.5(a) and 4.5(b) plot the amplitude spectrum of a typical trace in the conventionally datumed virtual SSP gather and the least-squares datumed SSP gather, respectively. The spectrum shows that LSD enhances the frequency content of the trace at both the low and high ends as this linearized inversion scheme acts as a deconvolution operator.

I further obtain the least-squares datumed virtual SSP gathers, in which I use the modified forward and adjoint datuming operators to include the datuming of VSP internal multiples. In Figure 4.4(c), the least-squares virtual SSP gather, obtained using the modified operators, shows a notable enhancement of the reflection events, especially the forth reflection event in the vicinity of the borehole. Figure 4.5(c) outlines the amplitude spectrum of a typical trace in this gather and suggests an enhancement of the frequency content and the deconvolution of the spectrum. In Figure 4.6, I show the convergence curve that plots the normalized data residual against the number of iterations. Using the proposed LSD framework, the normalized data residual curves before and after applying the modification of the operators to include the internal multiples decreased to about 1×10^{-2} after about 30 quasi-Newton iterations.

I then migrate both the conventional cross-correlation based datumed primaries and the LSD virtual SSP primaries. Figure 4.7(a) shows a diffraction-stack migrated image using the conventionally datumed SSP primaries. Clearly, the reflectors in this migrated section exhibit low-spatial resolution and the source wavelet is not properly deconvolved. Figure 4.7(b) is obtained by the diffraction-stack migration of the least-squares datumed virtual SSP primaries and shows a pronounced improvement of the quality of the migrated image. In other words, the reflectors look sharper and the source signature is well deconvolved as a result of LSD. I also migrated the least-squares datumed SSP gathers, which are obtained by the modified forward and adjoint datuming operators to include the datuming of the VSP internal multiples.

Figure 4.7(c) plots the diffraction-stack migrated image of the least-squares datumed primaries, obtained using the modified operators. It suggests a slight enhancement of the spatial resolution of the reflectors, especially the forth reflector near the borehole location. The results therefore demonstrates that LSD helps remarkably enhance the quality of the virtual SSP gathers, and the spatial resolution of the migrated images. The final images obtained by the diffraction-stack migration of the different least-squares datumed virtual SSP datasets in Figures 4.7(b) and 4.7(c) support this conclusion.

4.4 Conclusions

I proposed a linearized inversion framework, based on the reciprocity equation of the correlation and convolution types, in order to interferometrically transform VSP multiples to SSP primaries. I demonstrated how least-squares interferometric datuming can help deconvolve the source wavelet and acquisition fingerprints, suppress the datuming artifacts, and enhance the temporal resolution of the seismic reflectors in the virtual SSP gathers. I further imaged the virtual SSP primaries using Kirchhoff and the synthetic results show that imaging the highly-resolved least-squares datumed SSP primaries yields highly resolved migrated images compared with imaging the conventionally datumed virtual SSP primaries using cross-correlation. I further modified the forward modeling and adjoint datuming operators to include the transformation of interbed VSP multiples into SSP primaries in the linearized inversion scheme. The synthetic results shows the enhancement of the seismic events in both the least-squares datumed gather and the migrated image. I conclude that least-squares datuming can be an essential step to apply to the VSP data prior to imaging to obtain highly resolved virtual primaries, which can be subsequently imaged to obtain representative subsurface structures. I would expect this framework to work best should the VSP data contains significant amount of surface-related multiples.

Future work will consider incorporating deconvolution-type datuming operators such as cross-coherence in the linearized inversion framework. This is expected to yield more accurate virtual gathers obtained at a faster convergence rate than the ones obtained using the conventional reciprocity equations as forward modeling and adjoint datuming operators.

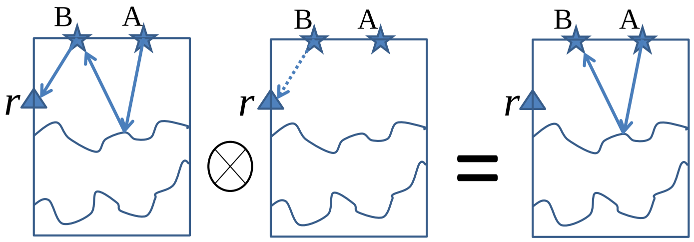

(a) Correlation-type datuming

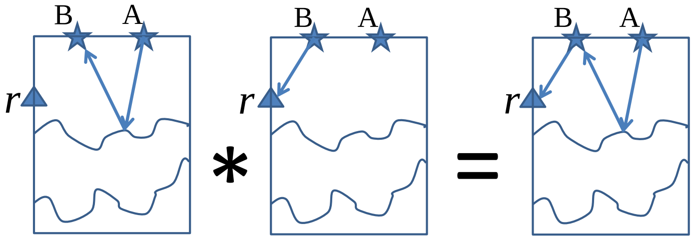

(b) Convolution-type dedatuming

Figure 4.1: Schematic ray diagrams: a) Cross-correlating a VSP surface-related multiple with a VSP direct wavefield yields a virtual surface-seismic primary. b) Convolving a surface-seismic primary with a VSP direct wavefield yields a VSP surface-related multiple.

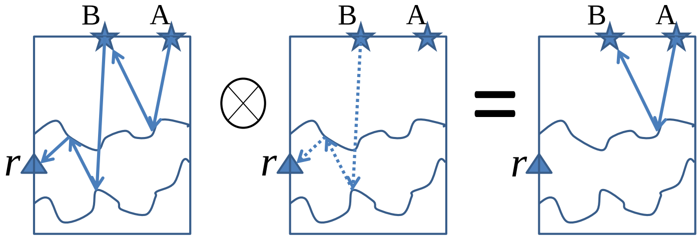

(a) Correlation-type datuming

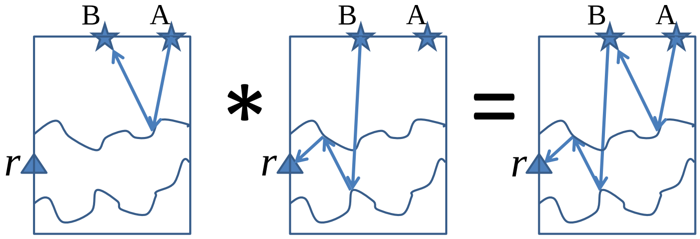

(b) Convolution-type dedatuming

Figure 4.2: Schematic ray diagrams for the modified operators: a) Cross-correlating a high-order interbed VSP multiple with a lower-order VSP multiples yields a virtual surface-seismic primary. b) Convolving a surface-seismic primary with a low-order VSP multiple yields a higher-order interbed VSP multiple.

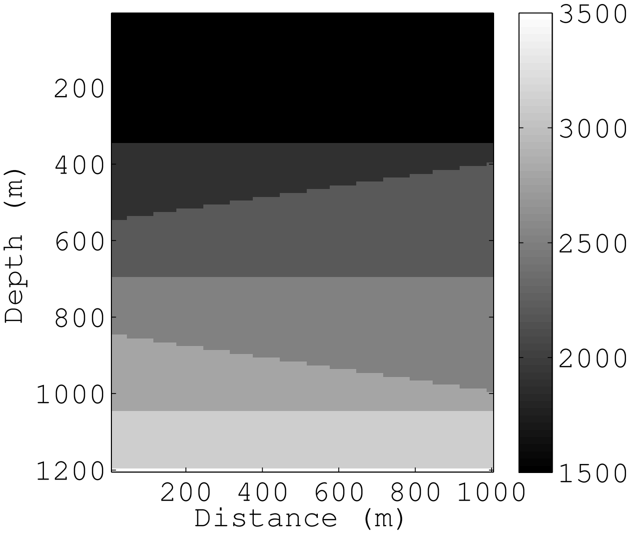

(a) True velocity model

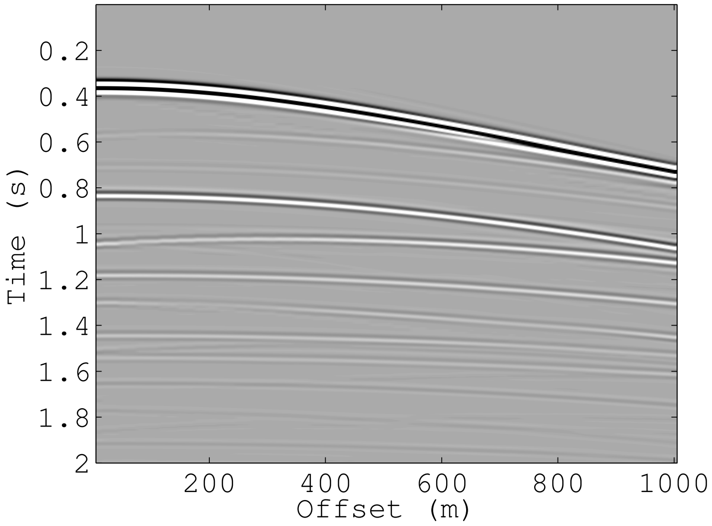

(b) A VSP common receiver gather

Figure 4.3: Synthetic finite-difference modeling: a) The true velocity model. b) A typical VSP common receiver gather.

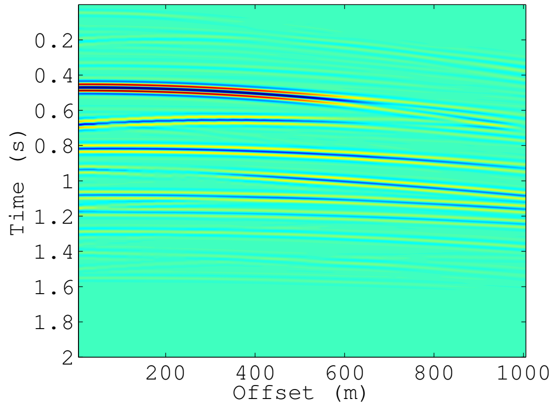

(a) Conventionally datumed SSP gather

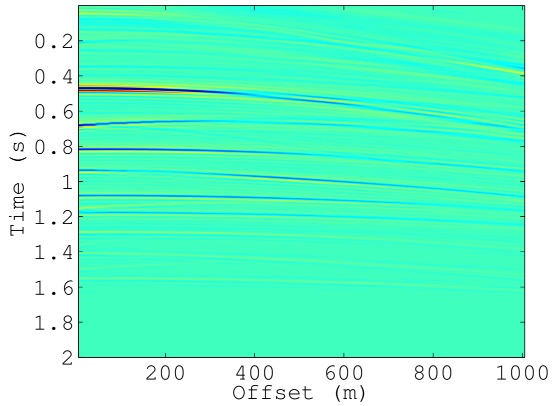

(b) Least-squares datumed SSP gather

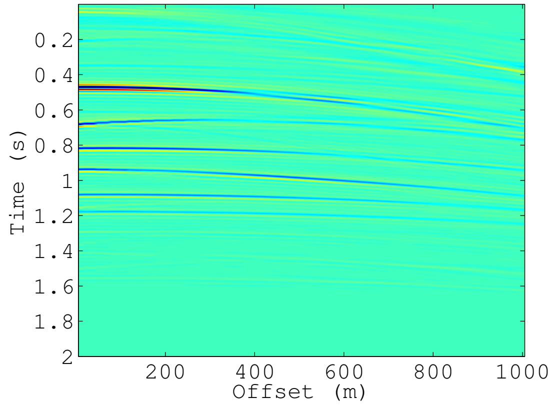

(c) Least-squares datumed SSP gather (modified operators)

Figure 4.4: Virtual SSP gathers: a) A conventional cross-correlation based datumed SSP gather. b) A least-squares datumed SSP gather. c) A least-squares datumed SSP gather obtained using the modified operators.

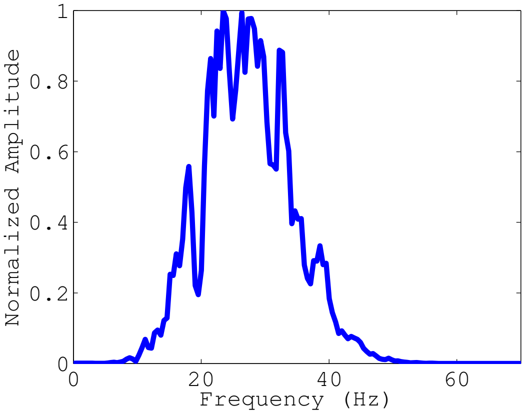

(a) Conventionally datumed trace amplitude spectrum

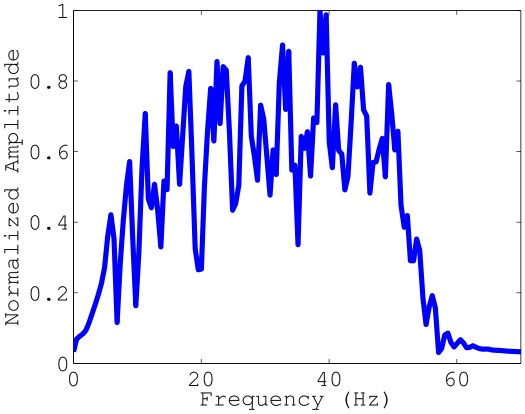

(b) Least-squares datumed trace amplitude spectrum

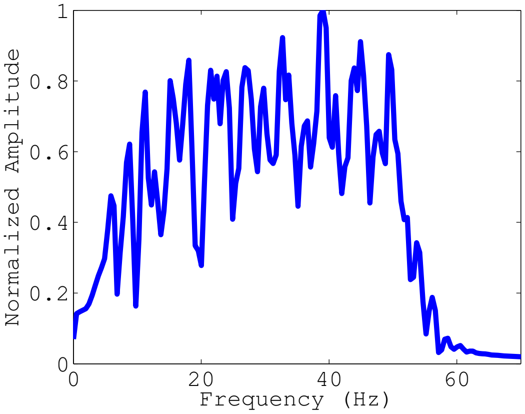

(c) Least-squares datumed trace amplitude spectrum (modified operators)

Figure 4.5: Amplitude spectrum: a) Amplitude spectrum of a conventionally datumed trace based on cross-correlation. b) Amplitude spectrum of a least-squares datumed trace. c) Amplitude spectrum of a least-squares datumed trace obtained using the modified operators.

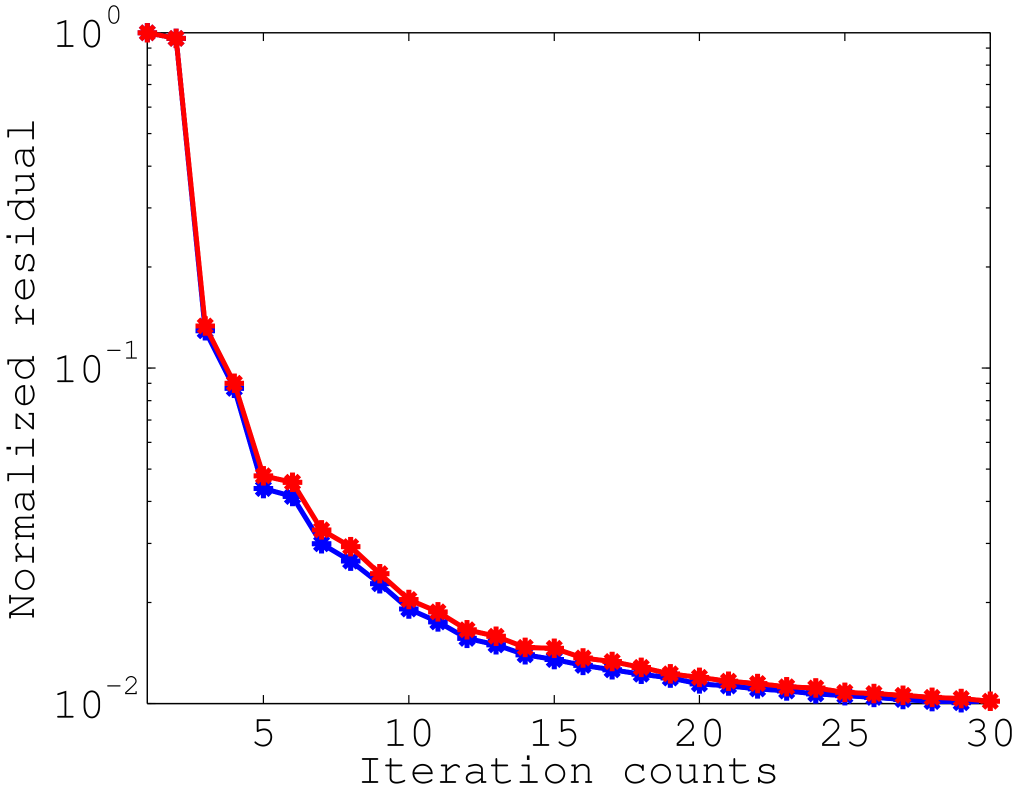

Figure 4.6: Convergence curves. The normalized data residual of the least-squares datumed data (blue) and the least-squares datumed data using the modified operators (red). After 30 quasi-Newton L-BFGS iterations, the normalized residual drops to about 1% in both cases.

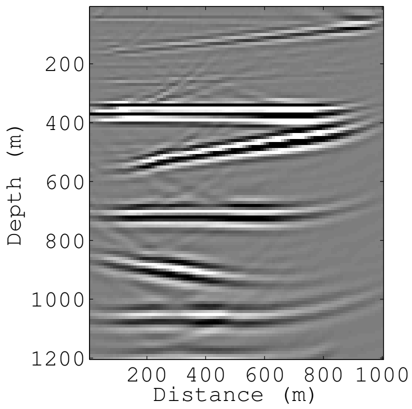

(a) Diffraction-stack image of conventionally datumed primaries

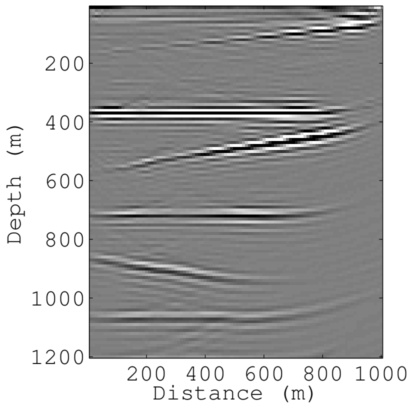

(b) Diffraction-stack image of least-squares datumed primaries

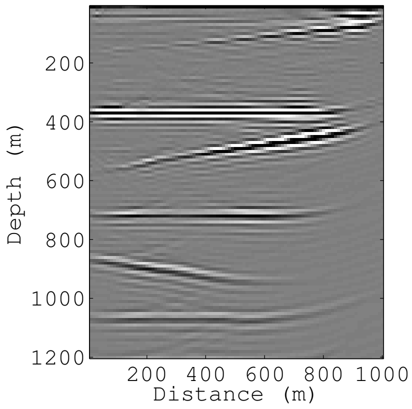

(c) Diffraction-stack image of least-squares datumed primaries (modified operators)

Figure 4.7: Migrated sections: a) Diffraction-stack migrated image of cross-correlation datumed virtual SSP primaries. b) Diffraction-stack migrated image of least-squares datumed virtual SSP primaries. c) Diffraction-stack migrated image of least-squares datumed virtual SSP primaries obtained using the modified operators.

Chapter 5

Least-squares generalized interferometric multiple imaging

The Generalized Interferometric Multiple Imaging procedure can be used to image duplex waves and other higher order internal multiples. Imaging duplex waves could help illuminate subsurface zones that are not easily illuminated by primary reflections such as vertical and nearly vertical fault planes, and salt flanks. To image first-order internal multiple, the Generalized Interferometric Multiple Imaging procedure consists of three datuming steps, followed by the application of the zero-lag cross-correlation imaging condition. However, the standard Generalized Interferometric Multiple Imaging procedure yields migrated images that suffer from low spatial resolution and migration artifacts caused by the acquisition geometry footprint, cross-talk noise between primaries and multiples, and limited bandwidth of the source wavelet. To alleviate these problems, I apply a least-squares Generalized Interferometric Multiple Imaging framework in which I formulate the first two steps of the standard Generalized Interferometric Multiple Imaging procedure for imaging duplex waves as a linearized inversion problem when imaging first-order internal multiples. Tests on synthetic datasets demonstrate the ability to localize subsurface scatterers in their actual subsurface positions, and delineate a vertical fault plane using the proposed method. I, also, demonstrate the robustness of the proposed framework when imaging the scatterers and the vertical fault plane with inaccurate migration velocities.

5.1 Introduction

Imaging internally scattered energy has the potential to reconstruct subsurface seismic reflectors that are poorly illuminated by single scattering seismic energy, such as vertical and nearly vertical fault planes, and salt flanks. Figure 5.1(a) illustrates schematically that a primary reflection has the tendency to illuminate a horizontally lying reflector. However, the single scattered specular ray is reflected away from the recording surface when it encounters a vertically lying reflector, as shown schematically in Figure 5.1(b). The vertical reflector is in fact illuminated by a doubly-scattered specular ray as schematically shown in Figure 5.1(c). Therefore, imaging this duplex energy would delineate the vertical reflector.

Youn and Zhou (2001) used a model-based estimate of internal multiples in their pre-stack depth imaging method. Malcolm et al. (2009) proposed a method to image internal multiple energy in which they migrate prismatic waves and other higher order multiples. Behura et al. (2012) imaged both single-scattered and internally multiple-scattered energy using an iterative procedure. Brown and Guitton (2005) proposed linearized inversion frameworks to migrate internal multiples. Other methods to image internally scattered waves include full wavefield migration (FWM) (Berkhout, 2012), reverse time migration for internal multiples (Liu et al., 2011b; Fleury, 2013), and auto-focusing imaging (da Costa Filho et al., 2015).

Seismic interferometry, also known as the virtual source method, is widely used to transform recorded seismic data from one acquisition geometry to another. The power of interferometric transformations lies in their ability to redatum seismic data without requiring the knowledge of the underlying velocity model. Seismic interferometry basically requires the cross-correlations, or convolutions of the recorded seismic traces, which act as natural wavefield extrapolators (Wapenaar and Fokkema, 2006; Schuster, 2009). One may also use this approach to extract the impulse response between receivers by making suitable combinations of the wavefields recorded at these receivers from different sources (Snieder et al., 2006). Recently, Zuberi and Alkhalifah (2014b) proposed the Generalized Interferometric Multiple Imaging procedure (GIMI) to image first-order and other higher order internal multiples. The GIMI framework, however, yields migrated images that suffer from low spatial resolution, migration artifacts, and cross-talk noise. These effects are caused by the limited recording aperture, the limited number of sources and/or receivers, the limited bandwidth of the source wavelet, and the interference between the primaries and multiples. Imaging first-order internal multiples using the GIMI framework consists of the following three datuming steps followed by applying the zero-lag cross-correlation imaging condition:

- An extrapolation-based datuming to redatum the surface points (i.e. sources/receivers) from the recording surface to the subsurface.
- A cross-correlation based datuming in which the extrapolated data is cross-correlated with the recorded surface seismic data.
- A forward extrapolation-based datuming to redatum the surface points (i.e. sources/receivers) from the recording surface to the subsurface trial image points.

Interferometric transformations or datuming of seismic data, based on the cross-correlations or extrapolation of seismic traces, deteriorates the quality of the final migrated image. The resulting images suffer from low spatial resolution due to the coarse source-receiver samplings, the limited acquisition aperture, and the distortion of the source wavelet, and the correlation artifacts caused by the cross-correlation or extrapolation steps. To alleviate these problems, I applied the least-squares datuming (LSD) framework in which I treated the wavefield extrapolation as an inversion problem to suppress the datuming artifacts and enhance the quality of the redatumed gathers (Ji, 1997; Ferguson, 2006; Xue and Schuster, 2008).

In this chapter, I propose a linearized inversion framework in which I formulate the first two datuming steps as a single least-squares problem. The aim is to enhance the spatial resolution, and suppress the cross-talk noise and migration artifacts when imaging prismatic waves. I apply both the conventional and the proposed-least-squares GIMI frameworks to two synthetic datasets. I, also, compare the resulting images with the least-squares migrated images based on single-scattering imaging. I lastly demonstrate the robustness of the proposed linearized inversion GIMI framework to reconstruct the synthetic models in the case of imaging the data with inaccurate migration velocities.

5.2 Method

Imaging first-order internal multiples using the standard generalized interferometric multiple imaging procedure consists of three datuming steps followed by the application of the zero-lag cross-correlation imaging condition to the datumed data (Zuberi and Alkhalifah, 2014b). The first datuming step is an extrapolation-based datuming to redatum the surface points (sources/receivers) from the recording surface to the subsurface. Mathematically, the first datuming step, presented here in the frequency domain under the high-frequency asymptotic approximation for simplicity, is defined as follows:

$$d_1(s,x,\omega) = \sum_g d(s,g,\omega)e^{-i\omega\tau_{gx}}, \tag{5.1}$$

where $d_1(s,x,\omega)$ is the first datumed data to the subsurface x for a particular source s and a particular frequency ω. $d(s,g,\omega)$ is the recorded surface data at receiver point g due to a source placed at point s for a particular frequency ω. The operation in equation (5.1) redatum the recorded trace from receiver points g's to the subsurface points x's. τ_{gx} is the traveltime from the receiver point g to the subsurface point g. Here, I am focusing on the kinematics of the redatumed wakefield.

The second datuming step in the generalized interferometric imaging procedure is a cross-correlation based-datuming in which the datumed data in the first step $d_1(s,x,\omega)$ is cross-correlated with the recorded data $d(s,g,\omega)$. Mathematically, the cross-correlation datuming step is given as follows:

$$d_2(g,x,\omega) = \sum_s d_1(s,x,\omega)d^*(s,g,\omega), \tag{5.2}$$

where $d^*(s,g,\omega)$ denotes the complex conjugate of the recorded trace in the frequency domain. $d_2(g,x,\omega)$ is the cross-correlated extrapolated data.

The last step in the GIMI procedure is a forward extrapolation datuming of $d_2(g,x,\omega)$ followed by the application of the zero-lag cross-correlation imaging condition. Mathematically, the datuming and imaging operations are defined as:

$$m(x) = \sum_\omega \sum_g d_2(g,x,\omega)e^{+i\omega\tau_{gx}}, \tag{5.3}$$

where $m(x)$ is the GIMI migrated image, which is illuminated by first-order internal multiples. The zero-lag cross-correlation imaging condition is obtained by summing over all frequencies.

Note that the first GIMI extrapolation step 5.1 is a backward propagation datuming while the third GIMI step is a forward extrapolation datuming 5.3. Therefore, the opposing signs of the traveltimes in these operators yield to the subtracting imaging condition in which the migration kernal traveltime contours traces out saddle-like surfaces as shown in Figure 5.2(a) (Schuster et al., 2004). The resulting contours tend to enhance the spatial resolution laterally; thus, it have more potential to image and delineate vertically lying reflectors than horizontal ones. In contrast, Figure 5.2(b) shows the migration kernals traveltime contours for the conventional summation imaging condition of primary reflections, which trace out elliptical surfaces (Schuster et al., 2004). These impulse response contours mainly delineates horizontally lying reflectors and are less sensitive to delineating vertical faults.

I propose a linearized inversion framework of the generalized interferometric multiple imaging procedure in which the first two datuming steps are formulated as a least-squares problem. The first two datuming steps are defined as follows:

$$d_2(g,x,\omega) = \sum_s \sum_{g'} [d_{input}(s,g',\omega) e^{-i\omega\tau_{g'x}}] d^*(s,g,\omega), \tag{5.4}$$

where $d_{input}(s,g',\omega)$ is the input data to these operators, which is the recorded data $d(s,g,\omega)$ in the standard GIMI procedure. The adjoint operation of the datuming steps in equation (5.4) is given by:

$$d_a(s,g,\omega) = \sum_x \sum_{g'} [d_2(g',x,\omega) d(s,g',\omega)] e^{+i\omega\tau_{gx}}. \tag{5.5}$$

Therefore, this forward modeling operation to predict the recorded data is obtained by the forward extrapolation from the subsurface points x's to the receiver points g's of the resulting dataset from the convolution of the cross-correlated extrapolated data $d_2(g',x,\omega)$ with the recorded data $d(s,g',\omega)$.

Using the datuming and forward modeling operators in equation (5.4) and (5.5), the first two datuming steps in the GIMI procedure can be formulate as a least-squares datuming problem in which I treat the wavefield extrapolation as a linearized inversion problem (Ji, 1997; Ferguson, 2006; Xue and Schuster, 2008). The least-squares cross-correlated extrapolated data $\mathbf{d_2^{ls}}$ can be obtained by solving iteratively the corresponding normal equation:

$$\mathbf{L}^\dagger \mathbf{L} \mathbf{d_2^{ls}} = \mathbf{L}^\dagger \mathbf{d}, \tag{5.6}$$

where $\mathbf{L}^\dagger$ denotes the datuming operator in equation (5.4), which linearly maps the recorded seismic data $\mathbf{d}$ to the cross-correlated extrapolated data. Similarly, $\mathbf{L}$ denotes the forward (i.e. adjoint $\mathbf{L}^\dagger$) operator in equation (5.5), which linearly maps the cross-correlated extrapolated data to the predicted recorded data. I use a conjugate gradient (CG) algorithm to solve the linear system in equation (5.6) and obtain the solution after 30 iterations. In the proposed least-squares GIMI framework, I use the least-squares solution of equation (5.6) as an input to the third GIMI step in equation (5.3). A notable liability of the proposed methodology is that it is memory intensive as it requires inverting wavefields rather than images in conventional least-squares migration of primary reflections. The computation of the datumed data, however, could easily be parallelized and split on different machines as a remedy to this memory-requirement problem.

5.3 Numerical Examples

I applied the proposed least-squares generalized interferometric multiple imaging procedure to two synthetic datasets and compared the results with the standard GIMI procedure results, and the least-squares migration results using only primary reflections. I also tested the robustness of the proposed methodology in the case of imaging the first-order multiples using inaccurate migration velocities. The two 50 by 100 grid size synthetic models shares the following acquisition parameters: 4 ms time sampling rate, $\Delta z = \Delta x = 30m$, 100 shot points and 100 receiver points along the earth surface, and a Ricker wavelet source function with a dominant frequency of 15 Hz.

The first example consists of two buried subsurface scatterers in a constant background velocity of 2000 m/s. The true reflectivity distribution is shown in Figure 5.3(a). I applied the standard three-step GIMI procedure to image the first-order internal multiples and plotted the result in Figure 5.3(b). The resulting image suffers from low spatial resolution, migration artifacts, and cross-talk noise, which are caused by the limited number of sources and/or receivers, the band-limited nature of the source wavelet, and the cross-talk between the recorded primaries and multiples. Therefore, the resulting image of the subsurface scatterers is heavily blurred and not well localized at their accurate subsurface positions. To alleviate these problems, I applied the proposed least-squared GIMI framework to image the first-order internal multiples and plotted the result in Figure 5.3(c). This migrated GIMI image shows a significant enhancement of the spatial resolution of the scatterers. In fact, the proposed linearized inversion GIMI framework helps suppress the migration artifacts and cross-talk noise, and deconvolve the source wavelet and acquisition footprint. For comparison, I also obtained the least-squares migrated image using primary reflections only and plotted the result in Figure 5.3(d).

To assess the robustness of the proposed methodology, I obtained the least-squares GIMI migrated images using 5% faster and slower migration velocities, respectively. I presented the results in Figure 5.4. Whereas imaging the scatterers with the faster velocity causes the scatterers to get blurred and shallower, imaging them with the slower velocity causes the defocused scatterers to be shifted deeper as shown in Figure 5.4(a) and 5.4(b), respectively.

The second synthetic model example consists of two layers with a separating vertical fault plane with a separating vertical fault plane as shown in Figure 5.5(a). The first layer has a velocity of 2900 m/s and the second layer has a velocity of 3000 m/s. I imaged the first-order internal multiple using the standard generalized interferometric multiple imaging procedure and plotted the result in Figure 5.5(b). The resulting migrated image is a smeared depiction of the true reflectivity distribution causing the vertical fault plane to be heavily blurred and poorly resolved. The smearing effect of the GIMI migrated section is caused mainly by the cross-talk noise between primaries and multiples, the limited bandwidth of the source wavelet, and the acquisition fingerprint.

To remedy these problems, I imaged the duplex waves using the proposed least-squares GIMI procedure and presented the result in Figure 5.5(c). The image shows the suppression of the cross-talk noise and the enhancement of the spatial resolution of the migrated GIMI image. Clearly, the vertical fault plane is highly resolved and more accurately delineated in its true subsurface position. The subtraction-type imaging condition used in the proposed GIMI framework tends to enhance the lateral resolution of the migrated image. For comparison, I plotted the least-squares migrated image using primary reflections only in Figure 5.5(d). The result demonstrate that imaging seismic data, under the single-scattering assumption, could mainly delineate horizontally-lying reflectors, which are mainly illuminated by primaries. In fact, the summation imaging condition used to image primaries enhances the vertical resolution of the migrated image. On the other hand, imaging prismatic waves could delineate vertically-lying fault planes, which are mainly illuminated by first-order internal multiples.

I then tested the robustness of the proposed linearized inversion GIMI framework in the case of imaging the recorded seismic data with inaccurate migration velocities. I migrated the first-order internal multiples using the proposed least-squares GIMI procedure with 5% faster and 5% slower migration velocities and plotted the result in Figure 5.6(a) and Figure 5.6(b), respectively. The resulting fault plane become slightly misplaced and defocused when imaging the first-order internal multiples with erroneous migration velocities. Whereas the fault plane is placed slightly shallower than its accurate position when imaging with the faster velocities, the fault plane is placed deeper when imaging with the slower ones. Therefore, the proposed method can yield robust migrated images using inaccurate migration velocities.

5.4 Conclusions

I demonstrated that imaging first-order internal multiples can help delineate vertically aligned seismic reflectors. I applied the standard three-step GIMI framework to selectively image scatterers, which are illuminated by first order internal multiples. I showed that the resulting images suffer from low spatial resolution due to cross-talk noise between primaries and multiples, migration artifacts, and acquisition fingerprint. Therefore, I proposed the least-squares GIMI framework to alleviate these problems. I formulated the first extrapolation-based datuming and cross-correlation based datuming steps in the standard GIMI procedure as a linearized inversion problem. I then obtained the least-squares GIMI images, which demonstrated the suppression of the cross-talk noise and migration artifacts, and the deconvolution of the source wavelet and acquisition fingerprint. They also show the enhancement of the spatial resolution of the final migrated GIMI images. The proposed method illustrated the capability of the linearized inversion to localize and resolve with high resolution subsurface scatterers, and a vertical fault plane. I also compared the result with the least-squares image using primary reflections. Whereas the least-squares migration of primaries enhances mainly horizontally aligned reflectors, the least-squares GIMI framework enhances and delineates vertically aligned reflectors. I lastly demonstrated the robustness of the proposed least-squares GIMI framework in the case of imaging the scatterers and the fault plane with erroneous migration velocities.

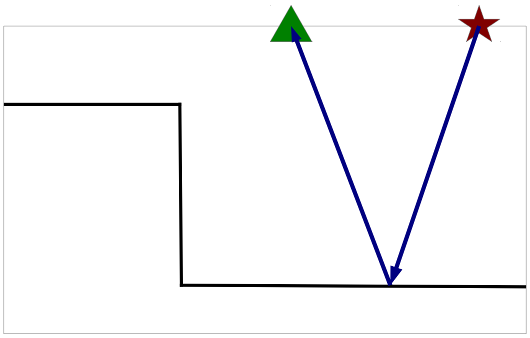

(a) Primary reflection from a horizontal reflector

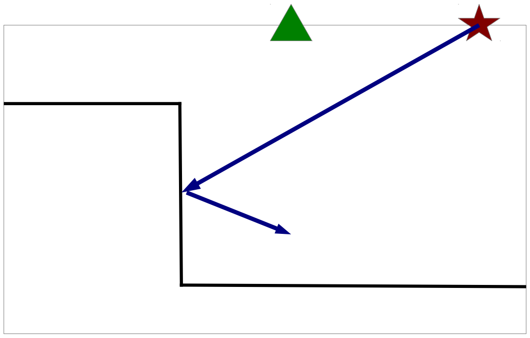

(b) Primary reflection from a vertical reflector

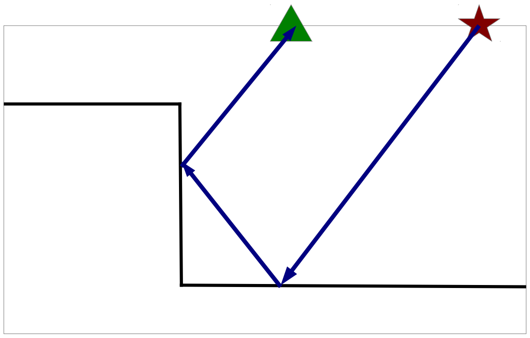

(c) Doubly-scattered reflection illuminates the vertical reflector

Figure 5.1: Schematic ray diagrams: a) A single-scattering reflected specular ray could potentially illuminate a horizontally lying reflector. b) A single-scattering specular reflected ray from a vertical reflector is diverted away from the recording surface. c) A doubly-scattered specular ray could potentially illuminate a vertically lying reflector.

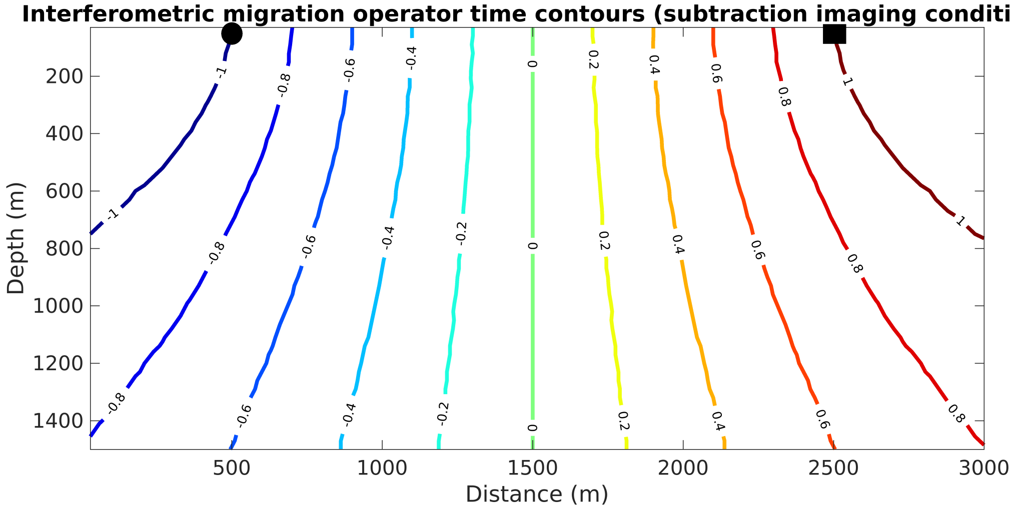

(a) Interferometric imaging impulse response traveltime contours

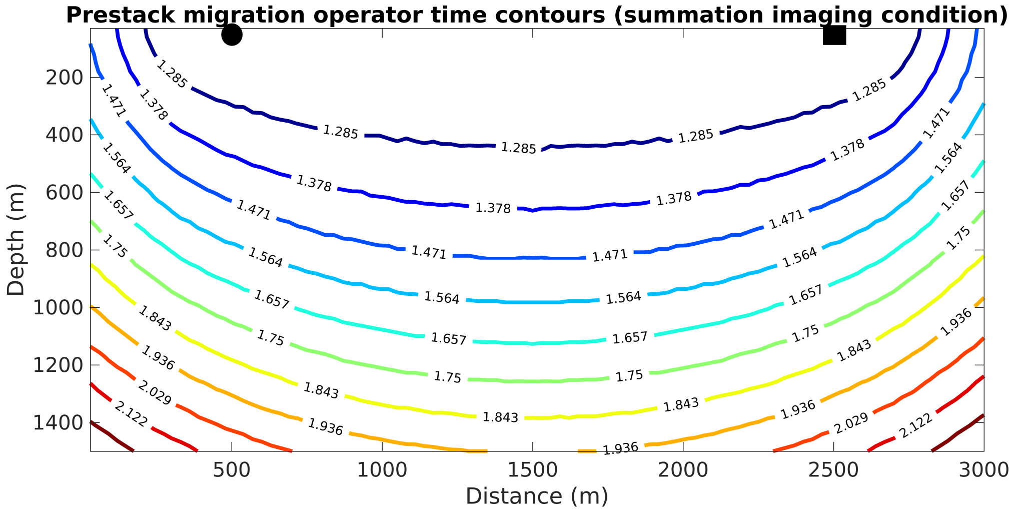

(b) Prestack imaging impulse response traveltime contours

Figure 5.2: Imaging conditions: a) The subtraction imaging condition in which the impulse response traveltime contours traces out saddle-like surfaces that are more sensitive to lateral variations. b) The summation imaging condition in which the impulse response traveltime contours traces out elliptical surfaces that are more sensitive to vertical variations. The subtraction imaging condition delineates vertically lying reflectors whereas the summation imaging condition enhances the resolution of horizontally lying reflectors. The circle denotes the source and the rectangle denotes the receiver and the velocity model has a constant velocity of 2000 m/s.

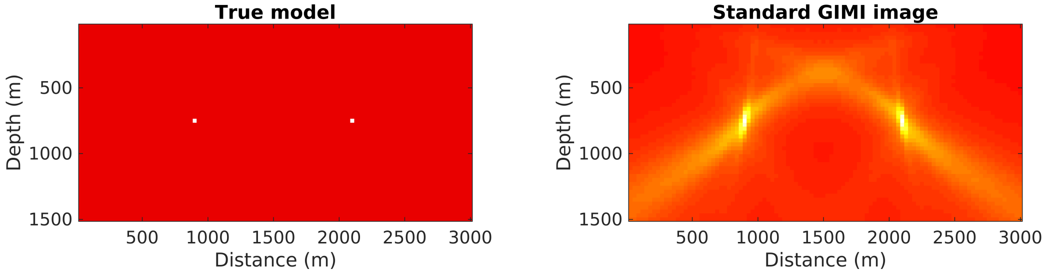

(a) True model

(b) Standard GIMI migrated section

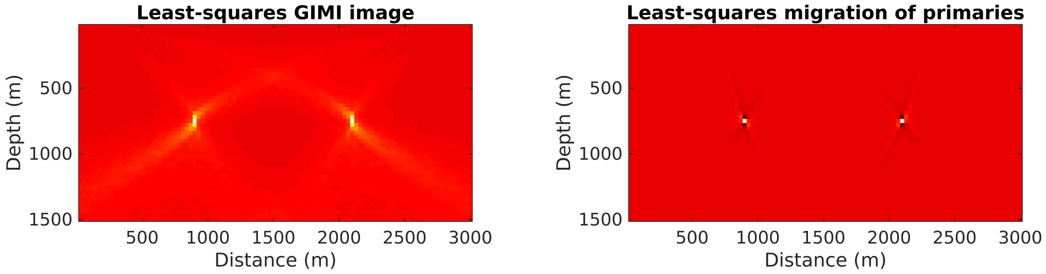

(c) Least-squares GIMI migrated section

(d) Least-squares migrated of primaries

Figure 5.3: Example 1: a) The true reflectivity model consists of two scatterers in a homogeneous background of 2000 m/s. b) The standard GIMI migrated section shows a heavily smeared depiction of the true reflectivity model. c) The least-squares GIMI migrated section shows the suppression of the artifacts, deconvolution of the acquisition fingerprint, and enhancement of the spatial resolution of the scatterers. d) The least-squares migration of primary reflections only.

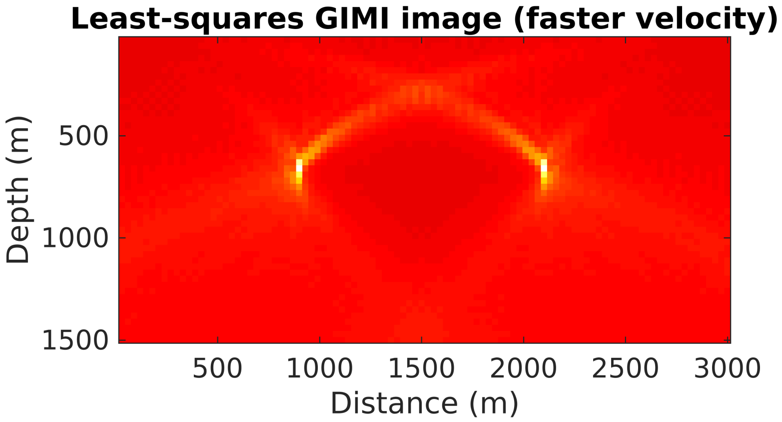
Least-squares GIMI image (faster velocity)

(a) Least-squares GIMI migrated image (faster velocity)

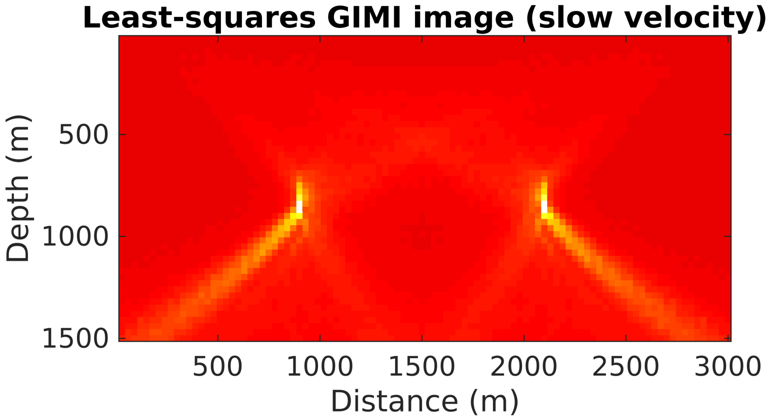
Least-squares GIMI image (slow velocity)

(b) Least-squares GIMI migrated image (slower velocity)

Figure 5.4: Example 1: Imaging the scatterers using the least-squares GIMI framework with: a) 5% faster migration velocity and b) 5% slower migration velocity

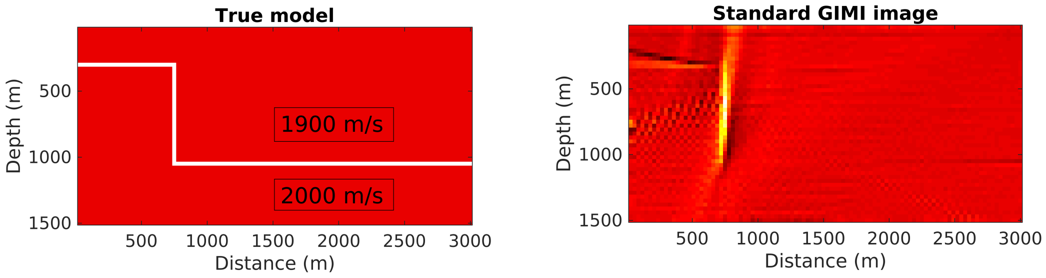

(a) True model (b) Standard GIMI migrated section

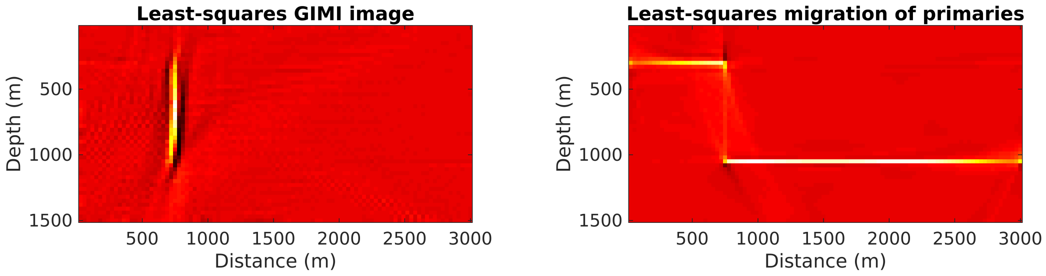

(c) Least-squares GIMI migrated section (d) Least-squares migrated of primaries

Figure 5.5: Example 2: a) The true reflectivity model consists of two layers with a separating vertical fault plane. b) The standard GIMI migrated section shows a heavily blurred depiction of the true reflectivity model. c) The least-squares GIMI migrated section shows the suppression of the artifacts, deconvolution of the acquisition footprint, and delineation of the vertical reflector. d) The least-squares migration of primary reflections only enhances mainly the horizontally lying reflector.

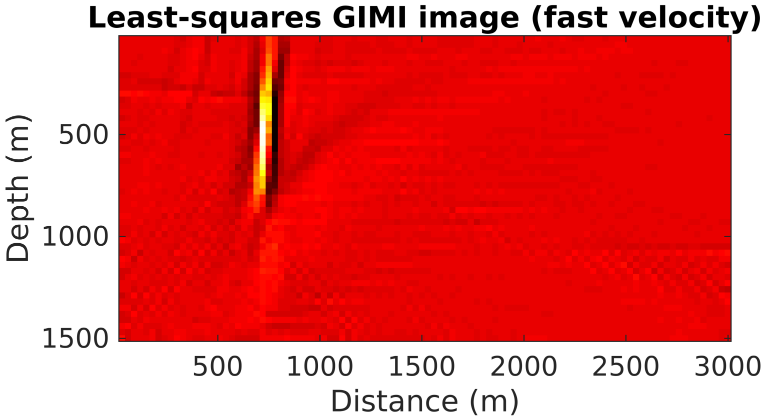

(a) Least-squares GIMI migrated image (faster velocity)

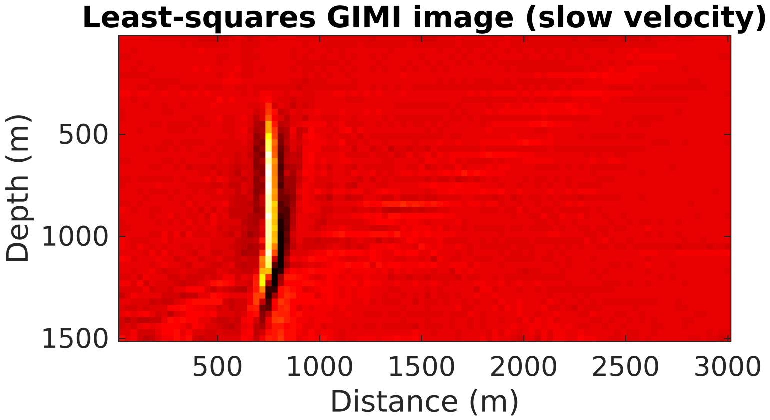

(b) Least-squares GIMI migrated image (slower velocity)

Figure 5.6: Example 2: Imaging the vertical fault plane using the least-squares GIMI framework with: a) 5% faster migration velocity and b) 5% slower migration velocity.

Chapter 6

Concluding Remarks and Future Work

6.1 Summary

The main focus of this dissertation was to propose and implement various cost-effective mathematical algorithms and methodologies to obtain highly resolved seismic migrated images. I first exploited the sparse nature of the subsurface reflectivity distribution and the fact that imaging multiples could potentially widen the illumination of the subsurface. Since subsurface reflectors and scatterers are sparse events in the subsurface, I could impose a constraint when inverting primaries that promotes the sparsity of the migrated images. I then developed algorithms to image multiples that would illuminate subsurface zones that are hardly illuminated by primaries when inverting primary reflection data only.

I focused on exploiting primary reflection seismic energy and formulated the seismic imaging of primaries problem as a sparse reconstruction problem, which could be solved by an L1-minimization algorithm. The synthetic results demonstrates that L1-minimization provides more focused images than the standard or least-squares migrated images in the case the noise level is relatively low and the migration velocity model is fairly accurate.

I also developed a new method to image internally multiply-scattered seismic waves, which have the potential to widen the illumination of the migrated images. I formulated this imaging problem as a least-squares problem. The results showed that the linearized inversion of internal multiples could delineate seismic reflectors, which cannot easily be delineated by primaries. The liability of this method is the need to perform a nested summation over the model space in the modeling step and to obtain an accurate estimation of the leas-squares migrated image of primaries.

I further studied the effect of least-squares interferometric datuming on imaging surface-related VSP multiples. The results demonstrated that the conventional cross-correlation based datuming method yields redatumed data that suffers from wavelet distortion, and correlation artifacts resulting in poorly migrated images. In contrast, the linearized interferometric inversion helps enhance the resolution of the redatumed data, and deconvolve the source wavelet, which in turn enhance the spatial resolution of the migrated sections.

I then extended the generalized interferometric multiple imaging procedure to image first-order internal multiples. I proposed a least-squares GIMI framework in which the first two datuming steps of the standard GIMI procedure are formulated as linearized inversion datuming steps. I constructed the optimal pairs of forward and adjoint operators to perform the least-squares GIMI more robustly and efficiently by formulating the first two datuming steps in the GIMI procedure as a least-squares datuming problem. The resulting images demonstrated the ability of the proposed least-squares GIMI framework to delineate a vertical fault plane with a higher resolution compared with the standard GIMI procedure. The results of the proposed least-squares GIMI framework were demonstrated to be robust in case of imaging the internal multiples with inaccurate migration velocities.

The proposed methods and algorithms could potentially be utilized to obtain seismic images with higher resolution. Also, the utilization of both internal and surface related multiples should be the next big step in the realm of seismic imaging as they provide the extra illumination that potentially could lead to new hydrocarbon discoveries.

6.2 Future work

The proposed methods were proven efficient and cost-effective when applied to synthetic data sets. It would be therefore important to first demonstrate the relevance of these methods and techniques for obtaining highly resolved images when applied to real data. Various realistic test cases need to be tested to assess the relevance and robustness of these methods. For instance, imaging a salt flank using the standard primary imaging migration or waveform inversion requires a wide acquisition coverage to capture the single reflection of that salt flank. The proposed method could allow the delineation of the salt flank with a shorter survey line using the proposed techniques of imaging of internal multiples.

On the technical side, one may consider combining the applied methodologies with data compression techniques using curvlets, seislets, or wavelets in order to compress the memory intensive wavefields that are used in the inversions. Also, one could take this study a step further and try to obtain velocity model updates by utilizing the GIMI framework in a full waveform inversion context. Obtaining velocity model updates from internal multiples could potentially help enhance the resolution of full waveform inversion and improve its convergence rate as one does not only rely on updates under the Born approximation assumption. Moreover, finding a corresponding GIMI kernel to update the velocity model to use it in a migration velocity analysis (MVA) framework is an essential step to make imaging multiples more robust and focus the smeared scatterers illuminated by seismic multiples in their true positions in case of imaging with inaccurate migration velocities. Another direction would be to combine the sparse reconstruction technology with the least-squares GIMI method in order to further enhance the spatial resolution of the GIMI migrated images and suppress the undesired artifacts. Another direction of improvement would be to linearize the third GIMI step and formulate it as a least-squares problem, which could further enhance the resolution of the final GIMI migrated section. Lastly, scaling the seismic imaging of multiples to 3D acquisition surveys and solving the problems using high performance computing (HPC) technologies would promote these technologies and make them applicable to comparable-size field datasets.

The work in this dissertation has been published or submitted to peer-reviewed journals, and presented as oral or poster presentations at international conferences. These are all listed in Appendix B in the appendices section.

REFERENCES

A Abubakar, TM Habashy, VL Druskin, D Alumbaugh, P Zhang, M Wilt, H Denaclara, E Nichols, and L Knizhnerman. A fast and rigorous 2.5 d inversion algorithm for cross-well electromagnetic data. *Proc. SEG Expanded Abstracts*, 24: 534–537, 2005.

O. Al-Hagan, S. Hanafy, and G. Schuster. Iterative supervirtual refraction interferometry. *GEOPHYSICS*, 79(3):Q21–Q30, 2014. doi: 10.1190/geo2013-0210.1. URL `http://dx.doi.org/10.1190/geo2013-0210.1`.

A. Aldawood, I. Hoteit, and T. Alkhalifah. The possibilities of compressed-sensing-based kirchhoff prestack migration. *GEOPHYSICS*, 79(3):S113–S120, 2014a. doi: 10.1190/geo2013-0271.1. URL `http://dx.doi.org/10.1190/geo2013-0271.1`.

A Aldawood, I Hoteit, G Turkiyyah, M Zuberi, and T Alkhalifah. Linearized least-square imaging of internally scattered data. In *76th EAGE Conference and Exhibition*, 2014b.

A. Aldawood, I. Hoteit, G. Turkiyyah, and T. Alkhalifah. Analysing the effects of least-squares datuming on VSP multiple imaging. In *77th EAGE Conference and Exhibition*, 2015. doi: 10.3997/2214-4609.201413362. URL `http://earthdoc.eage.org/publication/publicationdetails/?publication=81115`.

A. Alshuhail, A. Aldawood, and S. Hanafy. Application of super-virtual seismic refraction interferometry to enhance first arrivals: A case study from saudi arabia. *The Leading Edge*, 31(1):34–39, 2012. doi: 10.1190/1.3679326. URL `http://dx.doi.org/10.1190/1.3679326`.

Richard Aster, Brian Borchers, and Clifford Thurber. *Parameter Estimation and Inverse Problems (International Geophysics)*. Academic Press, har/cdr edition, January 2005. ISBN 0120656043. URL `http://www.amazon.com/exec/obidos/redirect?tag=citeulike07-20&path=ASIN/0120656043`.

Haim Avron, Andrei Sharf, Chen Greif, and Daniel Cohen-Or. l1-sparse reconstruction of sharp point set surfaces. *ACM Trans. Graph.*, 29(5):135:1–135:12, November 2010. ISSN 0730-0301. doi: 10.1145/1857907.1857911. URL `http://doi.acm.org/10.1145/1857907.1857911`.

Jyoti Behura, Kees Wapenaar, and Roel Snieder. Newton-marchenko-rose imaging. In *SEG Technical Program Expanded Abstracts 2012*, pages 1–6. Society of Exploration Geophysicists, 2012.

A. J. Berkhout. Combining full wavefield migration and full waveform inversion, a glance into the future of seismic imaging. *GEOPHYSICS*, 77(2):S43–S50, 2012. doi: 10.1190/geo2011-0148.1. URL `http://dx.doi.org/10.1190/geo2011-0148.1`.

A. J. (Guus) Berkhout and D. J. (Eric) Verschuur. Enriched seismic imaging by using multiple scattering. *The Leading Edge*, 35(2):128–133, 2016. doi: 10.1190/tle35020128.1. URL `http://dx.doi.org/10.1190/tle35020128.1`.

Pawan Bharadwaj, Gerard Schuster, Ian Mallinson, and Wei Dai. Theory of supervirtual refraction interferometry. *Geophysical Journal International*, 188(1): 263–273, 2012. ISSN 1365-246X. doi: 10.1111/j.1365-246X.2011.05253.x. URL `http://dx.doi.org/10.1111/j.1365-246X.2011.05253.x`.

A Borsic and A Adler. A primal–dual interior-point framework for using the l1 or l2 norm on the data and regularization terms of inverse problems. *Inverse Problems*, 28(9):095011, 2012.

Boris Boullenger* and Deyan Draganov. *Source reconstruction using seismic interferometry by multidimensional deconvolution*, pages 3804–3808. 2015. doi: 10.1190/segam2015-5856415.1. URL `http://library.seg.org/doi/abs/10.1190/segam2015-5856415.1`.

Filippo Broggini, Roel Snieder, and Kees Wapenaar. *Connection of scattering principles: Focusing the wavefield without source or receiver*, pages 3845–3850. 2011. doi: 10.1190/1.3628008. URL `http://library.seg.org/doi/abs/10.1190/1.3628008`.

Morgan P. Brown and Antoine Guitton. Least-squares joint imaging of multiples and primaries. *GEOPHYSICS*, 70(5):S79–S89, 2005. doi: 10.1190/1.2052471. URL `http://dx.doi.org/10.1190/1.2052471`.

S. Chen, D. Donoho, and M. Saunders. Atomic decomposition by basis pursuit. *SIAM Journal on Scientific Computing*, 20(1):33–61, 1998. doi: 10.1137/S1064827596304010. URL `http://epubs.siam.org/doi/abs/10.1137/S1064827596304010`.

S. Chen, D. Donoho, and M. Saunders. Atomic decomposition by basis pursuit. *SIAM Review*, 43(1):129–159, 2001. doi: 10.1137/S003614450037906X. URL `http://epubs.siam.org/doi/abs/10.1137/S003614450037906X`.

J. F. Claerbout. *Earth Soundings Analysis: Processing Versus Inversion.* Blackwell Science, 1992.

Jon F. Claerbout. Toward a unified theory of reflector mapping. *GEOPHYSICS*, 36 (3):467–481, 1971. doi: 10.1190/1.1440185. URL `http://dx.doi.org/10.1190/1.1440185`.

Jon F Claerbout and Sergey Fomel. *Image estimation by example: geophysical soundings image construction: multidimensional autoregression.* Stanford University, 2008.

E. Crase, A. Pica, M. Noble, J. McDonald, and A. Tarantola. Robust elastic nonlinear waveform inversion: Application to real data. *GEOPHYSICS*, 55(5):527–538, 1990. doi: 10.1190/1.1442864. URL `http://library.seg.org/doi/abs/10.1190/1.1442864`.

Andrew Curtis, Peter Gerstoft, Haruo Sato, Roel Snieder, and Kees Wapenaar. Seismic interferometryturning noise into signal. *The Leading Edge*, 25(9):1082–1092, 2006.

Carlos Alberto da Costa Filho, Matteo Ravasi, and Andrew Curtis. Elastic p- and s-wave autofocus imaging with primaries and internal multiples. *GEOPHYSICS*, 80(5):S187–S202, 2015. doi: 10.1190/geo2014-0512.1. URL `http://dx.doi.org/10.1190/geo2014-0512.1`.

Wei Dai. *Multisource Least-squares Reverse Time Migration.* PhD thesis, King Abdullah University of Science and Technology, 2012.

Wei Dai, Paul Fowler, and Gerard T. Schuster. Multi-source least-squares reverse time migration. *Geophysical Prospecting*, 60(4):681–695, 2012. ISSN 1365-2478. doi: 10.1111/j.1365-2478.2012.01092.x. URL `http://dx.doi.org/10.1111/j.1365-2478.2012.01092.x`.

D.L. Donoho. Compressed sensing. *Information Theory, IEEE Transactions on*, 52 (4):1289 –1306, april 2006. ISSN 0018-9448. doi: 10.1109/TIT.2006.871582.

Gaurav Dutta, Yunsong Huang, Wei Dai, Xin Wang, and Gerard T Schuster. Making the most out of the least (squares migration). *SEG Technical Program Expanded Abstracts 2014*, 2014.

Y.C. Eldar and G. Kutyniok. *Compressed Sensing: Theory and Applications*. Cambridge University Press, 2012. ISBN 9781107005587. URL `http://books.google.com.sa/books?id=TFJHYAAACAAJ`.

Robert J. Ferguson. Regularization and datuming of seismic data by weighted, damped least squares. *GEOPHYSICS*, 71(5):U67–U76, 2006. doi: 10.1190/1.2235616. URL `http://dx.doi.org/10.1190/1.2235616`.

Clement Fleury. Increasing illumination and sensitivity of reverse-time migration with internal multiples. *Geophysical Prospecting*, 61(5):891–906, 2013. ISSN 1365-2478. doi: 10.1111/1365-2478.12041. URL `http://dx.doi.org/10.1111/1365-2478.12041`.

S. Fomel and A. Guitton. Regularizing seismic inverse problems by model reparameterization using plane-wave construction. *GEOPHYSICS*, 71(5):A43–A47, 2006. doi: 10.1190/1.2335609. URL `http://library.seg.org/doi/abs/10.1190/1.2335609`.

Antoine Guitton. Shotprofile migration of multiple reflections. In *SEG Technical Program Expanded Abstracts 2002*, pages 1296–1299, 2002. doi: 10.1190/1.1816892. URL `http://library.seg.org/doi/abs/10.1190/1.1816892`.

Bowen Guo, Jianhua Yu, Yunsong Huang, Sherif M. Hanafy, and Gerard T. Schuster. Benefits and limitations of imaging multiples: Interferometric and resonant migration. *The Leading Edge*, 34(7):802–805, 2015. doi: 10.1190/tle34070802.1. URL `http://dx.doi.org/10.1190/tle34070802.1`.

Sherif M. Hanafy, Yunsong Huang, and Gerard T. Schuster. Benefits and limitations of imaging multiples: Mirror migration. *The Leading Edge*, 34(7):796–800, 2015. doi: 10.1190/tle34070796.1. URL `http://dx.doi.org/10.1190/tle34070796.1`.

Ruiqing He, Brian Hornby, and Gerard Schuster. 3D wave-equation interferometric migration of VSP multiples. *SEG Technical Program Expanded Abstracts*, pages

3442–3446, 2006. doi: 10.1190/1.2370249. URL `http://library.seg.org/doi/abs/10.1190/1.2370249`.

Felix J. Herrmann and Xiang Li. Efficient least-squares imaging with sparsity promotion and compressive sensing. *Geophysical Prospecting*, 60(4):696–712, 2012. ISSN 1365-2478. doi: 10.1111/j.1365-2478.2011.01041.x. URL `http://dx.doi.org/10.1111/j.1365-2478.2011.01041.x`.

Jun Ji. Least squares imaging, datuming, and interpolation using the wave equation. *SEP*, 75:121–135, 1997.

Zhiyong Jiang and Brian E. Hornby. A data-driven approach for 3D VSP multiple prediction. *SEG Technical Program Expanded Abstracts*, pages 3064–3068, 2007. doi: 10.1190/1.2793107. URL `http://library.seg.org/doi/abs/10.1190/1.2793107`.

Henning Khl and Mauricio D. Sacchi. Least?squares wave?equation migration for avp/ava inversion. *GEOPHYSICS*, 68(1):262–273, 2003. doi: 10.1190/1.1543212. URL `http://dx.doi.org/10.1190/1.1543212`.

E. Landa, W. Beydoun, and A. Tarantola. Reference velocity model estimation from prestack waveforms: Coherency optimization by simulated annealing. *GEOPHYSICS*, 54(8):984–990, 1989. doi: 10.1190/1.1442741. URL `http://library.seg.org/doi/abs/10.1190/1.1442741`.

R. LeBras and R. Clayton. An iterative inversion of back-scattered acoustic waves. *GEOPHYSICS*, 53(4):501–508, 1988. doi: 10.1190/1.1442481. URL `http://dx.doi.org/10.1190/1.1442481`.

Guo-Chang Liu, Xiao-Hong Chen, Jing-Ye Li, Jing Du, and Jia-Wen Song. Seismic noise attenuation using nonstationary polynomial fitting. *Applied Geophysics*, 8(1):18–26, 2011a.

Yike Liu, Xu Chang, Degang Jin, Ruiqing He, Hongchuan Sun, and Yingcai Zheng. Reverse time migration of multiples for subsalt imaging. *GEOPHYSICS*, 76(5):WB209–WB216, 2011b. doi: 10.1190/geo2010-0312.1. URL `http://dx.doi.org/10.1190/geo2010-0312.1`.

Rongrong Lu, Mark Willis, Xander Campman, Jonathan AjoFranklin, and M. Nafi Toksz. 2006.

Simon Luo, Dave Hale, et al. Separating traveltimes and amplitudes in waveform inversion. In *SEG Technical Program Expanded Abstracts*, volume 61, pages 27–34, 2013.

M. Lustig, D. L. Donoho, and J. M. Pauly. Rapid MR Imaging with "Compressed Sensing" and Randomly Under-Sampled 3DFT Trajectories. In *ISMRM*. ISMRM, 2006.

Michael Lustig, Juan M. Santos, Jin hyung Lee, David L. Donoho, and John M. Pauly. Application of compressed sensing for rapid mr imaging. In *in SPARS*, 2005.

Jitao Ma, Fengchang Yao, Xiaohong Chen, and Yang Liu. VSP multiple attenuation theory using srme technique. *SEG Technical Program Expanded Abstracts*, pages 3480–3484, 2011. doi: 10.1190/1.3627921. URL `http://library.seg.org/doi/abs/10.1190/1.3627921`.

Alison E. Malcolm, Bjrn Ursin, and Maarten V. De Hoop. Seismic imaging and illumination with internal multiples. *Geophysical Journal International*, 176(3): 847–864, 2009. ISSN 1365-246X. doi: 10.1111/j.1365-246X.2008.03992.x. URL `http://dx.doi.org/10.1111/j.1365-246X.2008.03992.x`.

Remco Muijs, Klaus Holliger, and Johan O. A. Robertsson. Prestack depth migration of primary and surfacerelated multiple reflections. In *SEG Technical Program Expanded Abstracts 2005*, pages 2107–2110, 2005. doi: 10.1190/1.2148128. URL `http://library.seg.org/doi/abs/10.1190/1.2148128`.

T. Nemeth, C. Wu, and G. Schuster. Least squares migration of incomplete reflection data. *GEOPHYSICS*, 64(1):208–221, 1999. doi: 10.1190/1.1444517. URL `http://library.seg.org/doi/abs/10.1190/1.1444517`.

J. Nocedal and S. J. Wright. *Numerical Optimization*. Springer, New York, 2nd edition, 2006.

William B. Pennebaker and Joan L. Mitchell. *JPEG Still Image Data Compression Standard*. Kluwer Academic Publishers, Norwell, MA, USA, 1st edition, 1992. ISBN 0442012721.

R Gerhard Pratt. Seismic waveform inversion in the frequency domain, part 1: Theory and verification in a physical scale model. *Geophysics*, 64(3):888–901, 1999.

A. Ribodetti, S. Operto, W. Agudelo, J.-Y. Collot, and J. Virieux. Joint ray + born least-squares migration and simulated annealing optimization for target-oriented quantitative seismic imaging. *GEOPHYSICS*, 76(2):R23–R42, 2011. doi: 10.1190/1.3554330. URL `http://dx.doi.org/10.1190/1.3554330`.

Gunter Roth and Albert Tarantola. Inversion of seismic waveforms using neural networks. In *SEG Technical Program Expanded Abstracts 1992*, pages 788–791. doi: 10.1190/1.1822218. URL `http://library.seg.org/doi/abs/10.1190/1.1822218`.

G. T. Schuster, J. Yu, J. Sheng, and J. Rickett. Interferometric/daylight seismic imaging. *Geophysical Journal International*, 157(2):838–852, 2004. doi: 10.1111/j.1365-246X.2004.02251.x. URL `http://gji.oxfordjournals.org/content/157/2/838.abstract`.

G.T. Schuster. *Seismic Interferometry*. Cambridge University Press, 2009. ISBN 9780521871242. URL `http://books.google.com.sa/books?id=SZ2kITQgDxAC`.

Jianming Sheng. Migrating multiples and primaries in cdp data by crosscorrelogram migration. In *SEG Technical Program Expanded Abstracts 2001*, pages 1297–1300, 2001. doi: 10.1190/1.1816333. URL `http://library.seg.org/doi/abs/10.1190/1.1816333`.

R. Snieder, M. Y. Xie, A. Tarantola, and A. Pica. Retrieving both the impedance variations and background velocity in reflection seismics using leastsquares waveform inversion. In *SEG Technical Program Expanded Abstracts 1988*, pages 1070–1072. doi: 10.1190/1.1892169. URL `http://library.seg.org/doi/abs/10.1190/1.1892169`.

Roel Snieder, Jon Sheiman, and Rodney Calvert. Equivalence of the virtual-source method and wave-field deconvolution in seismic interferometry. *Phys. Rev. E*, 73:066620, Jun 2006. doi: 10.1103/PhysRevE.73.066620. URL `http://link.aps.org/doi/10.1103/PhysRevE.73.066620`.

Yaxun Tang. Least-squares migration of incomplete data sets with regularization in the subsurface-offset domain. *Stanford Exploration Project*, 125:159–174, 2006.

Yaxun Tang. Target-oriented wave-equation least-squares migration/inversion with phase-encoded hessian. *GEOPHYSICS*, 74(6):WCA95–WCA107, 2009. doi: 10.1190/1.3204768. URL `http://dx.doi.org/10.1190/1.3204768`.

D.S. Taubman and M.W. Marcellin. *Jpeg2000: Image Compression Fundamentals, Standards, and Practice*. The Springer International Series in Engineering and Computer Science Series. Springer-Verlag GmbH, 2002. ISBN 9780792375197. URL `http://books.google.com.sa/books?id=czmyZeqmJIEC`.

J. Trzasko and A. Manduca. Highly undersampled magnetic resonance image reconstruction via homotopic l_0 -minimization. *Medical Imaging, IEEE Transactions on*, 28(1):106 –121, jan. 2009. ISSN 0278-0062. doi: 10.1109/TMI.2008.927346.

Ning Tu and Felix J. Herrmann. Fast least-squares imaging with surface-related multiples: Application to a north sea data set. *The Leading Edge*, 34(7):788–794, 2015. doi: 10.1190/tle34070788.1. URL `http://dx.doi.org/10.1190/tle34070788.1`.

E. van den Berg and M. P. Friedlander. SPGL1: A solver for large-scale sparse reconstruction, June 2007. http://www.cs.ubc.ca/labs/scl/spgl1.

E. van den Berg and M. P. Friedlander. Probing the pareto frontier for basis pursuit solutions. *SIAM Journal on Scientific Computing*, 31(2):890–912, 2008. doi: 10.1137/080714488. URL `http://link.aip.org/link/?SCE/31/890`.

D. J. Verschuur and A. J. Berkhout. From removing to using multiples in closed-loop imaging. *The Leading Edge*, 34(7):744–759, 2015. doi: 10.1190/tle34070744.1. URL `http://dx.doi.org/10.1190/tle34070744.1`.

Bao-Li Wang, Guang-Ming Zhu, and Jing-Huai Gao. Joint interferometric imaging of walkaway vsp data. *Applied Geophysics*, 7(1):41–48, 2010. ISSN 1672-7975. doi: 10.1007/s11770-010-0004-3. URL `http://dx.doi.org/10.1007/s11770-010-0004-3`.

J. Wang and M. Sacchi. High-resolution wave-equation amplitude-variation-with-ray-parameter (avp) imaging with sparseness constraints. *GEOPHYSICS*, 72(1): S11–S18, 2007. doi: 10.1190/1.2387139. URL `http://dx.doi.org/10.1190/1.2387139`.

K. Wapenaar and J. Fokkema. Green's function representations for seismic interferometry. *GEOPHYSICS*, 71(4):SI33–SI46, 2006. doi: 10.1190/1.2213955. URL `http://dx.doi.org/10.1190/1.2213955`.

Kees Wapenaar, Filippo Broggini, and Roel Snieder. Creating a virtual source inside a medium from reflection data: heuristic derivation and stationary-phase analysis. *Geophysical Journal International*, 190(2):1020–1024, 2012. ISSN 1365-246X.

doi: 10.1111/j.1365-246X.2012.05551.x. URL `http://dx.doi.org/10.1111/j.1365-246X.2012.05551.x`.

Kees Wapenaar, Joost van der Neut, Jan Thorbecke, Filippo Broggini, Evert Slob, and Roel Snieder. Seismic reflection imaging, accounting for primary and multiple reflections. In *EGU General Assembly Conference Abstracts*, volume 17, page 10470, 2015.

Mandy Wong, Biondo Biondi, and Shuki Ronen. Imaging with multiples using least-squares reverse time migration. *The Leading Edge*, 33(9):970–976, 2014.

Yanwei Xue and Gerard T. Schuster. Least squares datuming with the wave equation. *SEG Technical Program Expanded Abstracts*, pages 2366–2370, 2008. doi: 10.1190/1.3059354. URL `http://library.seg.org/doi/abs/10.1190/1.3059354`.

Zhiping Yang, Jeshurun Hembd, Hui Chen, and Jing Yang. Reverse time migration of multiples: Applications and challenges. *The Leading Edge*, 34(7):780–786, 2015. doi: 10.1190/tle34070780.1. URL `http://dx.doi.org/10.1190/tle34070780.1`.

O. Yilmaz. *Seismic Data Analysis*. Society of Exploration Geophysicists, 2001. doi: 10.1190/1.9781560801580. URL `http://library.seg.org/doi/abs/10.1190/1.9781560801580`.

Oong K. Youn and Huawei Zhou. Depth imaging with multiples. *GEOPHYSICS*, 66 (1):246–255, 2001. doi: 10.1190/1.1444901. URL `http://dx.doi.org/10.1190/1.1444901`.

Shi Yu, Léon-Charles Tranchevent, Bart De Moor, and Yves Moreau. Kernel-based data fusion for machine learning. *Studies in Computational Intelligence: Springer Berlin Heidelberg*, 2011.

Yu Zhang and Lian Duan. Predicting multiples using a reverse time demigration. In *SEG Technical Program Expanded Abstracts 2012*, chapter 704, pages 1–5. 2012. doi: 10.1190/segam2012-0520.1. URL `http://library.seg.org/doi/abs/10.1190/segam2012-0520.1`.

M. A. H. Zuberi and Tariq Alkhalifah. Generalized internal multiple imaging (gimi) using feynman-like diagrams. *Geophysical Journal International*, 197(3):1582–1592, 2014a. doi: 10.1093/gji/ggt527. URL `http://gji.oxfordjournals.org/content/197/3/1582.abstract`.

M. A. H. Zuberi and Tariq Alkhalifah. Generalized internal multiple imaging. *GEOPHYSICS*, 79(5):S207–S216, 2014b. doi: 10.1190/geo2013-0287.1. URL `http://dx.doi.org/10.1190/geo2013-0287.1`.

MAH Zuberi and T Alkhalifah. Selective interferometric imaging of internal multiples. In *75th EAGE Conference & Exhibition incorporating SPE EUROPEC*, 2013.

APPENDICES

A Gradient-based Optimization

The L2-norm least-squares misfit objective function has the form:

$$J = \frac{1}{2}\left\| \mathbf{\Psi}\mathbf{m} - \mathbf{d^{obs}} \right\|_2^2, \tag{A.1}$$

where $\mathbf{\Psi}$ is a linear operator, which maps the observed data vector $\mathbf{d^{obs}}$ to the vector of model parameters $\mathbf{m}$. This objective function is minimized and the model parameters are updated after each iteration by moving along the negative gradient direction (i.e. the direction of maximum descent) to obtain the next iterate using a steepest descent algorithm. The gradient is obtained by back-projecting the data residual vector onto the model space using the adjoint operator. However, the steepest descent algorithm suffers from slow convergence since it only utilizes the gradient direction at every iteration (Aster et al., 2005). A better search direction is the quasi-Newton direction, which utilizes both the gradient direction and the curvature information of the objective function characterized by the Hessian matrix. An approximate Hessian can be deduced by monitoring how the gradient changes with respect to the model update after each iteration.

The BFGS quasi-Newton algorithm, named after its discoverers Broyden, Fletcher, Goldfarb, and Shanno, uses an approximate Hessian $\mathbf{B}_k$ in finding the new search direction at the kth iteration given by the projection of the gradient vector onto the column space of the inverse Hessian approximation (i.e. -$\mathbf{B}_k^{-1}\nabla_{\mathbf{m}}J_k$) (Nocedal and Wright, 2006). $\mathbf{B}_k$ is a symmetric positive definite matrix that is updated after each iteration and ∇J_k is the gradient direction evaluated at the current iterate. In the steepest descent algorithm, the search direction is the negative gradient direction with $\mathbf{B} = \mathbf{I}$. The BFGS formula for updating the approximate Hessian is given by:

$$\mathbf{B}_{k+1} = \mathbf{B}_k - \frac{\mathbf{B}_k\mathbf{s}_k\mathbf{s}_k^T\mathbf{B}_k}{\mathbf{s}_k^T\mathbf{B}_k\mathbf{s}_k} + \frac{\mathbf{y}_k\mathbf{y}_k^T}{\mathbf{y}_k^T\mathbf{s}_k}, \tag{A.2}$$

where $\mathbf{s}_k = \mathbf{m}_{k+1} - \mathbf{m}_k$ and $\mathbf{y}_k = \nabla_{\mathbf{m}}J_{k+1} - \nabla_{\mathbf{m}}J_k$. Notice that the difference between $\mathbf{B}_{k+1}$ and $\mathbf{B}_k$ is a rank-two matrix. The major advantage of the quasi-Newton BFGS algorithm is that it does not require the calculation of second derivatives, utilizing the gradient changes to obtain curvature information (Nocedal and Wright, 2006). The reflectivity model is updated by moving along this quasi-Newton direction as follows:

$$\mathbf{m}_{k+1} = \mathbf{m}_k - \alpha\mathbf{B}^{-1}\nabla_{\mathbf{m}}J_k, \tag{A.3}$$

where α is a scalar value that determines how much one should move along the quasi-Newton direction and it could be obtained by a numerical line search scheme (Nocedal and Wright, 2006).

"*fmincon*" is a MATLAB function, included in the MATLAB's optimization toolbox, to compute the minimum of a scalar objective function of several variables. It implements a limited-memory L-BFGS optimization algorithm, which is based on the BFGS optimization algorithm. L-BFGS is used to solve large-scale problems, whose approximate Hessian matrices of size $n \times n$ where n is the number of knowns, cannot be computed and/or stored (Nocedal and Wright, 2006). Instead, they store just few vectors of length n that represents the Hessian approximation implicitly. I utilized it here to solve the single-scattering and the double-scattering imaging problem.

The stopping criteria of the optimization is when the number of function evaluations reaches a maximum of 50 evaluations.

B Papers Submitted and Under Preparation

The list of peer-reviewed journal papers are as follows:

○ Aldawood A, Hoteit I, and Alkhalifah T, "The possibilities of compressed-sensing-based Kirchhoff prestack migration", *Submitted to GEOPHYSICS*, Published, May. 2014, GEOPHYSICS, 79(3), S113-S120. doi: 10.1190/geo2013-0271.1

○ Aldawood A, Hoteit I, Turkiyyah G, and Alkhalifah T, "The possibilities of least-squares migration of internally scattered seismic energy", *Submitted to GEOPHYSICS*, Published, July. 2015, 80(4), S93-S101. doi: 10.1190/geo2014-0436.1

○ Aldawood A, Hoteit I, Turkiyyah G, and Alkhalifah T, "The application of least-squares interferometric datuming for imaging VSP surface-related multiples", *Submitted to GEOPHYSICS*, Under revision.

○ Aldawood A, Hoteit I, and Alkhalifah T, "Least-squares Generalized Interferometric Multiple Imaging", *Submitted to GEOPHYSICS*, Under revision.

The list of the conference papers are as follows:

- Aldawood A, Hoteit I, and Alkhalifah T, "Compressed-sensing Application - Prestack Kirchhoff Migration", *Submitted to the 75th EAGE Conference and Exhibition 2013*, Presented as a poster presentation, 2013. DOI: 10.3997/2214-4609.20130612
- Aldawood A, Hoteit I, and Alkhalifah T, "The possibilities of compressed sensing based migration", *Submitted to the SEG Technical Program Expanded Abstracts 2013*,

Presented as an oral presentation, 2013: pp. 3900-3904. doi: 10.1190/segam2013-0828.1

- Aldawood A, Hoteit I, Turkiyyah G, Zuberi M, and Alkhalifah T, “Linearized Least-square Imaging of Internally Scattered Data”, *Submitted to the 76th EAGE Conference and Exhibition 2014*, Presented as an oral presentation, 2014. DOI: 10.3997/2214-4609.20141160
- Aldawood A, Hoteit I, Turkiyyah G, Zuberi M, and Alkhalifah T, “The possibilities of linearized inversion of internally scattered seismic data”, *Submitted to the SEG Technical Program Expanded Abstracts 2014*, Presented as an oral presentation, 2014: pp. 3737-3741. doi: 10.1190/segam2014-0497.1
- Aldawood A, and Hoteit I, “Investigating the Effect of Least-square Datuming on Imaging VSP Multiples”, *Submitted to the 3rd EAGE Workshop on Borehole Geophysics*, Presented as an oral presentation, 2015. DOI: 10.3997/2214-4609.201412200
- Aldawood A, Hoteit I, Turkiyyah G, and Alkhalifah T, “A Study on the Effect of Least-squares Datuming on VSP Multiple Imaging”, *Submitted to the EAGE interferometry workshop 2015*, Presented as a poster presentation, 2015. DOI: 10.3997/2214-4609.201413577
- Aldawood A, Hoteit I, Turkiyyah G, and Alkhalifah T, “Analysing the Effects of Least-squares Datuming on VSP Multiple Imaging”, *Submitted to the 77th EAGE Conference and Exhibition 2015*, Presented as a poster presentation, 2015. DOI: 10.3997/2214-4609.201413362
- Aldawood A, Alshuhail Abdulrahman , Alshuhail Abdullatif, and Hoteit I, “Enhancing the signal-to-noise ratio of sonic waveforms by Interferometric stacking”, *Submitted to the ICE Barcelona 2016 Technical Program*, Presented as an oral presentation, 2016: pp. 141-141. doi: 10.1190/ice2016-6440588.1
- Aldawood A, Hoteit I, and Alkhalifah T, “Least-squares Generalized Interferometric Multiple Imaging”, *Submitted to the 78th EAGE Conference and Exhibition 2016*,

Presented as an oral presentation. DOI: 10.3997/2214-4609.201601202

- Aldawood A, Hoteit I, and Alkhalifah T, “The linearized inversion of the generalized interferometric multiple imaging”, *Submitted to SEG Technical Program Expanded Abstracts 2016*, : pp. 4250-4254. doi: 10.1190/segam2016-13680101.1 . to be presented as an oral presentation.